Georgi Kovachev, BSc

3D Photoacoustic Tomography with a Line Detector Array

MASTERARBEIT

Zur Erlangung des akademischen Grades

Master of Science

Masterstudium Nanophysik

eingereicht an der

Technischen Universität Graz

Betreuer

Ao. Univ. Prof. Dr. Günther Paltauf

Institut für Physik

Universität Graz

Graz, September 2016

EIDESSTATTLICHE ERKLÄRUNG

Ich erkläre an Eides statt, dass ich die vorliegende Arbeit selbstständig verfasst, andere als die angegebenen Quellen/Hilfsmittel nicht benutzt, und die den benutzten Quellen wörtlich und inhaltlich entnommenen Stellen als solche kenntlich gemacht habe. Das in TUGRAZonline hochgeladene Textdokument ist mit der vorliegenden Masterarbeit identisch.

Datum	Unterschrift

ABSTRACT

Photoacoustic imaging has seen great development in the last two decades and is one of the fastest developing imaging techniques, used for characterization of materials and biological samples. It is based on generation of sound waves at structures with preferential optical absorption inside an object upon illumination with pulsed electromagnetic radiation. Due to high resolution and non-ionizing character of the incident light it is more frequently used in medicine and also in basic research.

An array consisting of 64 unfocused piezoelectric line sensors made out of PVDF film is presented, characterized and used for measurements of various biological and non-biological samples. The sensor elements placed on a half cylindrical surface can detect simultaneously signals generated in an object, positioned near their centre axis in a water bath. By making use of the filtered back-projection algorithm it is possible to obtain a projection of the energy density distribution along a line. A full three-dimensional image is obtained after rotating the sample and applying the inverse Radon transform on the line projections.

The biggest advantage of the presented setup is the fast data acquisition. With four times averaging and a laser pulse repetition rate of 20 Hz, data for a full 3D image can be collected in less than two minutes. The device was able to resolve absorbers with a size on the order of $200\mu m$. By combining the light source with an optical parametric oscillator (OPO) the multispectral imaging capabilities of the device are shown by taking measurements on specimens with defined spectral absorption characteristics. Three dimensional images of isolated mouse organs were also obtained and it was possible to visualise their internal blood vessel structure.

Zusammenfassung

Die photoakustische Bildgebung hat sich in den letzten zwei Jahrzehnten stark weiter entwickelt und wird immer häufiger für die Charakterisierung von Materialien und biologischen Proben verwendet. Sie basiert auf der Erzeugung von Schallwellen in Objekten mit guten Absorptionseigenschaften durch Beleuchtung mit elektromagnetischer Strahlung. Wegen der möglichen hohen Auflösung und der nicht-ionisierenden Natur des einfallenden Lichtes findet das Verfahren häufig Anwendung in der Medizin und in der Grundlagenforschung.

In dieser Arbeit wird ein Array bestehend aus 64 nicht-fokussierten piezoelektrischen Liniensensoren aus PVDF-Folie präsentiert, charakterisiert und für Messungen von biologischen Proben und nicht-biologischen Materialien verwendet. Die Detektoren, positioniert auf dem Mantel eines mit Wasser gefüllten Halbzylinders, können Signale von einem eingetauchten Objekt gleichzeitig registrieren. Durch die gefilterte Rückprojektionsmethode ist es möglich, Projektionen von der Energiedichteverteilung entlang einer Linie zu bekommen. Durch Drehen der Probe und Anwendung der inversen Radon-Transformation auf die Linienprojektionen ist es möglich ein 3D Bild zu rekonstruieren.

Der größte Vorteil des präsentierten Setups ist die schnelle Datenaufnahme. Bei vier Mittelungen und einer Wiederholungsrate des Laserpulses von 20 Hz wird die Datenmenge - für eine 3D-Bildrekonstruktion - innerhalb von zwei Minuten aufgenommen. Objekte mit einer Größe von 200µm konnten mit dem Gerät aufgelöst werden.

Durch Kombination mit einem optisch parametrischen Oszillator (OPO) wurde die Möglichkeit der multi-spektralen Bildgebung des Aufbaus gezeigt. 3D Bilder von isolierten Mausorganen wurden rekonstruiert und deren Blutgefäßstrukturen visualisiert

Danksagung

Als Erstes möchte ich mich bei meinem Betreuer Dr. Günther Paltauf für seine ständige Unterstützung und für die geleistete Hilfe bedanken. Dankbar bin ich auch für seine Geduld und für die Möglichkeit in seiner Arbeitsgruppe arbeiten zu dürfen.

Ein großes Dankeschön auch an Dr. Robert Nuster, der immer hilfsbereit war und mich bei der Erfassung dieser Arbeit unterstützt hat.

Danken möchte ich auch dem Studiendekan Dr. Roland Würschum, der immer offen war und mir bei Schwierigkeiten geholfen hat.

Vielen Dank richte ich auch an meine Studienkollegen Monika Grafl, Thomas Vorauer, Patrick Rupp, Paul Torke, Eveline Ochensberger und Eva Grünwald und an alle anderen in der Gruppe, die mich motiviert haben und für mich da waren. Danke für die aufregenden Diskussionen und das gute Arbeitsklima.

Ich möchte mich auch besonders bei Tobias Binder und Michael Treml bedanken. Ohne euch hätte ich mein Studium nie geschafft. Vielen Dank für die tollen Erinnerungen und die schönen Zeiten. Danke an Veronika Kirilova für die ständige Unterstützung und für die Kraft, die du mir gebracht hast, alle Schwierigkeiten zu bewältigen.

Nicht an letzter Stelle möchte ich mich gern bei meinem Bruder und meinen Eltern bedanken. Ihr habt immer an mich geglaubt und ohne euch wäre dieses Studium nicht möglich gewesen.

CONTENTS

1 INTRODUCTION

Alexander Bell first described the generation of acoustic waves by illuminating an object with modulated sunlight in his report in 1880[1]. Before the development of suitable light sources (lasers) however, little progress was achieved in the field of photoacoustic imaging. Today photoacoustic tomography (PAT) arises as a promising imaging technique of biological tissues and samples ex- and in-vivo. It is based on the photoacoustic effect, where the energy of the absorbed light, originating from a pulsed laser source, is converted into acoustic energy. This results in the generation and emission of acoustic pressure waves, which serves as a basis for the reconstruction of high-resolution images. Such high resolution can be achieved because the scattering of acoustic waves in tissue is much less than that of light. Recent studies in the field show great success and prove that PA imaging could have an important role in future clinical diagnostics. The fact that signals, measured by PA sensors, strongly depend on the optical absorption characteristics of samples, led to experiments, where vascular structures were imaged by using the contrast provided by oxygen-poor and oxygen-rich hemoglobin[2][3]. Examples in literature can be found, where authors made use of the spectral dependence of the optical absorption of some tissue chromophores, which provide high imaging contrast when irradiated by a light wavelength at their absorption peak. An example for this is the determination of lipid deposits in atheromatous plaques, having an absorption peak at 1210 nm [4]. PA imaging is also used for tumor detection [5] and cellular imaging [6]. In recent years great progress has been made in breast cancer detection and characterisation [7], [8], due to the development and use of new and promising contrast agents [3].

In this work the main focus will fall on Photoacoustic Tomography (PAT, also known as optoacoustic tomography). After a brief discussion of the theoretical background of photoacoustics in general and how the initial pressure signal is generated, a method for three-dimensional photoacoustic imaging using an array of piezoelectric line sensors, arranged on a half-cylindrical surface, will be demonstrated. An overview of the algorithm used for three-dimensional image reconstruction will be presented. It is done in two steps and combines the universal back-projection method and the inverse Radon transform. Afterwards information about the sensors used and how they function will be given.

In the third chapter a display of the experimental setup will be provided, followed by a theoretical and experimental characterization of the bandwidth and resolution of the tomograph.

After discussion of the corrections made for the sensitivity of each line sensor and their positions with respect to the centre of the cylindrical surface, the strengths of the device will be shown in obtaining an image of objects, containing absorbing structures of several hundred micrometers size, within several minutes. Samples used here have biological as well as non-biological character. The intensity of the measured signal can be enhanced by using contrast agents, which strongly absorb light in different regions of the light spectra, for which an experimental proof will be provided.

In the final chapter, a conclusion will be made and an outlook on future developments will be given. The main goal here was to show that such an array of line sensors can be used for fast characterization of materials and biological samples.

2 THEORETICAL BACKGROUND

The conversion of absorbed light energy into acoustic energy leads to generation of pressure waves, but only under certain conditions. This is discussed in the first chapter (2.1) of this section.

Section 2.2 familiarizes us with the methods of photoacoustic imaging. First a brief review of photoacoustic microscopy and the experimental setups used will be presented, followed by a more detailed description of photoacoustic tomography, on which the main focus of this thesis will fall. Afterwards it will be shown how the initial pressure distribution is reconstructed from the measured data. The two steps in which the three-dimensional image is obtained – universal back projection and inverse Radon transform, are discussed in more detail. A few detector geometries will then be pointed out and compared with each other, showing the pros and cons of each of them.

Section 2.3 shows us the different ways of sensing pressure waves. Optical methods are worth mentioning, but here the main focus will fall on sensors based on the piezoelectric effect. Different types of piezoelectric sensors and the signals that we acquire from them are compared and discussed.

It is also worth mentioning that speed of sound can change in different materials, affecting the propagation of sound waves. Temperature has also some influence on the sound speed. The dependence of the speed of sound on different factors is shown in section (2.4) of this chapter.

In the last two sections the behaviour of pressure waves at interfaces is discussed, followed by some signal processing techniques used during reconstruction of the 3D images.

2.1 Photoacoustic effect

The photoacoustic effect is based on the generation of pressure waves due to absorption of electromagnetic energy in a medium. Directing sufficiently short laser pulses onto a light absorber leads to a local temperature rise with negligible thermal diffusion. The rapid heating results in a pressure increase within the sample. After relaxation of this thermoelastic pressure a sound wave is emitted, which can be measured by an ultrasonic transducer. The measured signal contains information about the size of the acoustic sources and their location.

Absorption of light in different structures is described by Beer-Lambert Law. It states that the intensity of the absorbed light will decrease exponentially with the depth and can be expressed as follows:

$$I(z) = I_{inc} e^{-\mu_a z} \tag{1}$$

Here μ_a is the absorption coefficient in the medium, and I_{inc} is the incident intensity, which is given by the following relationship:

$$I_{inc} = \frac{4P}{d_B^2 \pi} \tag{2}$$

Here P is the laser power and the denominator is an expression for the illuminated area. d_B stands for the beam diameter.

P is related to the energy and duration of the laser pulses.

$$P = \frac{Q_p}{t_p} \tag{3}$$

The conversion of electromagnetic energy into acoustic energy is most efficient, when the conditions of thermal and stress confinement are satisfied. The thermal confinement states that the pulse duration t_p should be shorter than the thermal relaxation time t_{therm}, which is given by the following equation:

$$t_p < t_{therm} \approx \frac{\delta^2}{\lambda_w} \tag{4}$$

Here δ is the characteristic size of the heated structure (penetration depth of incident light) and λ_w is the thermal diffusivity. When the thermal confinement is satisfied, no heat diffuses to the surroundings during the laser pulse, which means that the temperature rise is maximal in the irradiated volume and proportional to the absorbed light energy. By making the assumption that all of the energy, absorbed by the sample, is turned into heat, we can express the temperature rise as follows:

$$\Delta T = \frac{Q_p}{V.\rho.C_p} = \frac{W}{\rho.C_p} \tag{5}$$

where ρ is the medium density, C_p is the heat capacity at constant pressure and $W = {}^{Q_p}/_{V}$ is the volumetric energy density.

The stress confinement states that the pulse duration should be shorter than the acoustic relaxation time t_{ac} and is given by:

$$t_p < t_{ac} = \frac{\delta}{c} \tag{6}$$

where c denotes the speed of sound. Acoustic relaxation time is the time that the generated pressure wave needs to travel through the illuminated volume. By satisfying the stress confinement, volume expansion during heating can be neglected.

It is usually true that $t_{ac} < t_{therm}$, so when the stress confinement is satisfied, the thermal confinement is also fulfilled. When a pressure wave is created under stress confinement conditions the whole absorbed energy is stored in the illuminated region and the temperature rise and pressure rise in that region are maximal giving rise to a wave with maximum amplitude.

The local volume expansion at a certain position $\vec{r}$ can be written as:

$$\frac{\Delta V}{V} = -kp(\vec{r}) + \beta T(\vec{r}) \tag{7}$$

Here β is the thermal coefficient of volume expansion and k denotes the compressibility, which can be expressed by:

$$k = \frac{C_p}{\rho c^2 C_v} \tag{8}$$

Assuming that the stress confinement condition (2) is fulfilled and there is no change in the volume ($\Delta V=0$) we can get the local pressure rise p_0 by rewriting equation (7) as [9]:

$$p_0(\vec{r}) = \frac{\beta T(\vec{r})}{k} \tag{9}$$

Taking (5) into account leads to an expression for the pressure that relaxes as an acoustic wave:

$$p_0(\vec{r}) = \frac{\beta}{k.\rho.C_V} W = \Gamma W \tag{10}$$

Γ is called the Grüneisen parameter and is dimensionless.

The generation of photo-acoustic waves and their propagation through a medium can be described by the general form of the opto-acoustic wave equation:

$$\left(\Delta^2 - \frac{1}{{v_s}^2}\frac{\partial^2}{\partial t^2}\right) p(\vec{r}, t) = -\frac{\beta}{k{v_s}^2}\frac{\partial^2 T(\vec{r},t)}{\partial t^2} \tag{11}$$

Here $p(r, t)$ and $T(r, t)$ describe the pressure and temperature rise respectively at position r and time t. If (4) and (6) are satisfied for the short laser pulse then it is true that:

$$pC_V \frac{\partial T(\vec{r},t)}{\partial t} = H(\vec{r},t) \tag{12}$$

where H is a function that describes the deposited thermal energy per unit volume and time and is called the heating function. By taking (12) and putting it into (11) we obtain an equation with the following form:

$$\left(\Delta^2 - \frac{1}{{v_s}^2}\frac{\partial^2}{\partial t^2}\right) p(\vec{r},t) = -\frac{\beta}{C_p}\frac{\partial H(\vec{r},t)}{\partial t} \tag{13}$$

Here the left hand side describes how the wave propagates and the right hand side is a representation of the source term. It is important to mention that photoacoustic waves will be generated only if the heating function changes with time.

The forward solution of this equation can be found by using a Green's function [10-13], which leads to the following Poission integral for the photo-acoustic pressure:

$$p(\vec{r},t) = \frac{\beta}{4\pi c_p}\int_{V'} d\vec{r}' \frac{1}{|\vec{r}-\vec{r}'|} \left[\frac{\partial H(\vec{r}',t')}{\partial t'}\right]_{t'=t-|\vec{r}-\vec{r}'|/v_s} \tag{14}$$

(14) can be used for calculating the pressure produced from an arbitrary absorbing source.

2.2 Photoacoustic imaging

For Photoacoustic imaging two techniques can be used. The first one is photoacoustic microscopy, which is based on a scanning, focused ultrasonic transducer. It is used to visualize small tumors, blood vessels and cells with a resolution ranging to several hundred nanometers.

The second method, called Photoacoustic tomography, uses an array of unfocused ultrasonic transducers to scan the sample for a large solid angle. A reconstruction method is needed to be able to obtain the initial pressure distribution, from which the acoustic wave is originating from. With this technique a spatial resolution ranging from tens of micrometers to a couple of hundred micrometers can be achieved. The main focus here will fall on photoacoustic tomography

2.2.1 Photoacoustic microscopy

Photoacoustic microscopy uses a focused ultrasonic transducer aligned with the pulsed laser beam that raster-scans the sample to form directly an image from the depth-resolved signals. The axial resolution of PAM is determined by the frequency response of the ultrasonic transducer and the imaging depth and the lateral resolution by the product of the point spread functions of the light illumination and acoustic detection [14].

Two work regimes can be distinguished. The first uses a tightly focused laser beam, where the size of the spot is very small compared to the acoustic focus. Maximum penetration depth is limited by the strong optical scattering. About 1mm penetration inside tissues can be achieved [15]. This regime is called optical resolution photoacoustic microscopy. Limiting factor for the lateral resolution here is the numerical aperture of the optical objective. Higher NA results in better lateral resolution, but it decreases the imaging depth. To achieve higher penetration depths a more weakly focused laser beam can be used, resulting in a larger illumination area than the acoustic focus. This is the basis of acoustical resolution photoacoustic microscopy. Since the acoustic waves are less scattered in tissue than light waves a better penetration depth can be achieved with AR-PAM – about 4 mm. The main factor that accounts for the resolution here is the acoustic focusing.

The applications of this technique are numerous. For example Zhang, H.F. *et.al.*imaged hemoglobin oxygen saturation variations in single vessels *in vivo*[2] . They imaged also skin melanoma and its surrounding blood vessel structures in vivo using multi-wavelength PAM [16]. More examples include imaging of acute thermal burns to evaluate burn depth [17] or imaging of living mouse brain vasculature using hollow gold nanospheres as contrast agent [3].

2.2.2 Photoacoustic tomography

Photoacoustic tomography is based on scanning a sample with an unfocused ultrasonic transducer: There are two basic concepts for practical realization of this principle. The first is a single ultrasonic transducer, which is moved around the sample. The second uses an ultrasonic transducer array, where the acoustic waves are acquired simultaneously at many positions outside the object. For an exact reconstruction a large number of array elements (several hundred) is necessary. A combination of both concepts uses an array with a relatively low number of elements (around 100 or less), where the sample is rotated relative to the array to increase the effective number of sensor positions. Short laser pulses, with a typical duration in the range of 10 ns, irradiate the sample volume, where they are absorbed and thermoelastic pressure waves are generated. The main aim here is to recover the initial pressure distribution (9) from the time-dependent ultrasonic signals that were detected by the ultrasonic transducers. By combining the time-varying signal data, collected by each sensor, and applying a reconstruction algorithm we can obtain the full 3D image.

The spatial resolution of PAT depends strongly on the bandwidth of the acoustic signal that reaches the detector. The use of nanosecond laser pulses usually results in broadband ultrasonic waves with frequencies up to hundred megahertz. The propagation of the wave through the sample, however, leads to frequency dependent attenuation, the strength of which depends on the sample type. This limits the high frequency content of the acoustic wave, which determines the spatial resolution limit that can be achieved. Spatial resolution scales with depth, which means the deeper the acoustic wave is generated the stronger the attenuation of its high frequency content will be.

Limited view can also be a limiting factor for the spatial resolution. The data collected over a solid angle less than 4π (for 3D imaging) is usually insufficient, which will result in artefacts in the final image. Spatial resolution is also influenced by the characteristics of the transducers. The detector aperture has a big influence on the lateral resolution of the system [18]. Best case scenario is to use small-aperture unfocused detectors with a large acceptance angle. Both, axial and lateral resolutions are strongly affected by the bandwidth of the transducers [18].

PAT can be used to observe tumour growth [5], organ perfusion [19] and cardiovascular dynamics [20] in mice. PAT can also be used for breast cancer detection [7, 8] or to study peripheral joints [21].

2.2.2.1 Image reconstruction

For image reconstruction a variety of methods can be used. For example time-reversal methods use models that re-emit the detected waves from every detector position in reversed temporal order until the initial pressure distribution is achieved [22, 23]. An iterative method can be used that is based on a model to simulate numerically the PA signals. Starting from a first estimate, the initial pressure distribution is adjusted iteratively until the difference between measured PA signals and pressure signals calculated for the current estimate is minimized [24].

The tomograph used in this work uses piezoelectric line detectors. The advantages of line-shaped compared to point-like detectors will be discussed in section 2.3. Line detectors integrate the incoming pressure waves along one dimension in space, requiring a special reconstruction method. To obtain a complete, 3D reconstruction, integrated (or projected) signals for many orientations of the line detector array relative to the sample have to be recorded. This is done by rotating the sample about an axis perpendicular to the line orientation. The reconstruction is done in two steps: In the first step the universal back-projection method is used to obtain for each orientation of the sample a projection of the initial pressure distribution in a plane perpendicular to the line detectors. Then the inverse Radon transform is used to retrieve the 3D initial pressure distribution from the complete set of two-dimensional projections.

2.2.2.1.1 Universal Back-Projection method

We can write down the acoustic signal recorded by an ideal point transducer, positioned at $\overrightarrow{r'}$ as [25]:

$$p(\overrightarrow{r'}, t) = \frac{\partial}{\partial t}\left[\frac{t}{4\pi}\iint_{\left|\overrightarrow{r'}-\vec{r}\right|=v_s t} p_0(\vec{r})\, d\Omega\right] \qquad (15)$$

where c_s is the speed of sound and $d\Omega$ is the solid angle element with respect to the position $\vec{r}'$. In other words, this equation tells us that the signal detected by the transducer at time t comes from a spherical surface with radius $c_s t$, the center of which is located at the detector position $\vec{r}'$.

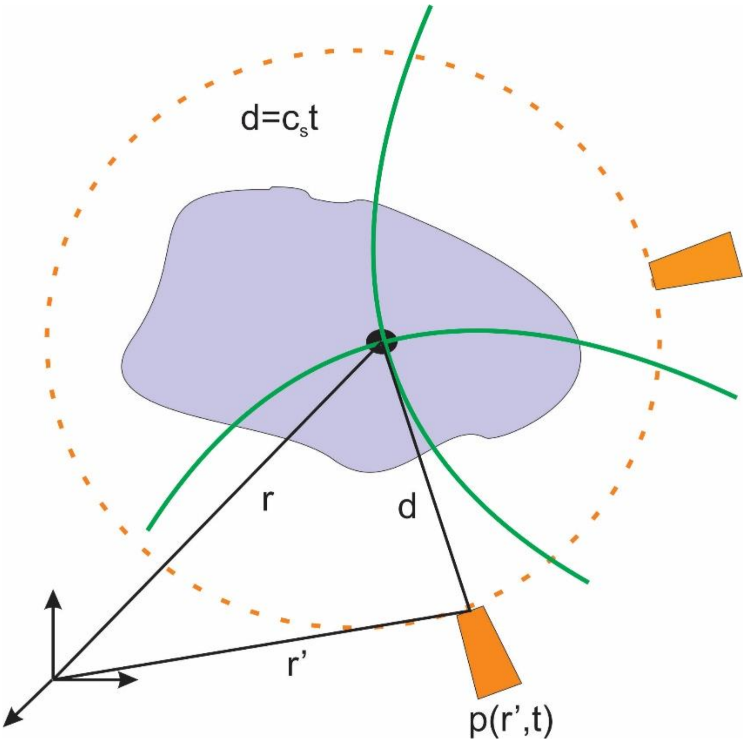

Figure.1 Signal generation and image reconstruction in photoacoustic tomography. The signal generated at detector position r' is an integral of the initial pressure distribution over a spherical surface with radius $c_s t$. For back projection, a signal measured at time $t = d/c_s$ is distributed over a spherical surface with radius d and the results for all detector positions are summed up.

The universal back projection algorithm can be expressed with the following formula and gives an exact reconstruction for the planar, cylindrical and spherical geometries as derived by Xu and Wang [25, 26].:

$$p_0{}^{(N)}(\vec{r}) = \int_{\Omega} \left(b(\overrightarrow{r'}, t = \frac{d}{c_s})\right) \frac{d\Omega}{\Omega} \tag{16}$$

It gives and estimation for the initial pressure $p_0{}^{(N)}(\vec{r})$, where $b\left(\overrightarrow{r'}, t\right)$ is the back projection data, derived from the measured pressure data at position $\overrightarrow{r'}$of the detector, $d\Omega/\Omega$ is a weighing factor for each back-projection and Ω is the solid angle of the sensor surface (the surface over which the detectors are distributed) with respect to a reconstruction point at position $\vec{r}$. N here is a measure of the dimensionality.

For the 3 dimensional case $N = 3$[27], the back-projection quantity $b(\overrightarrow{r'}, t)$ and the weighing factor $d\Omega$ are given by:

$$b(\overrightarrow{r'}, t) = -2t^2 \frac{\partial}{\partial t} (\frac{p(r', t)}{t}), \quad d\Omega = \frac{\mathrm{dS_0}}{d^2} \frac{\boldsymbol{\acute{n}_0}.\mathbf{d}}{d} \tag{17}$$

Here, $\mathrm{dS_0}$ is the surface element on the detection surface. $\boldsymbol{\acute{n}_0}$ is the normal unit vector that is perpendicular to $\mathrm{S_0}$ and points in the direction of the sample.

In the case of line sensors, which integrate the incoming pressure field along the direction of the line, the problem is two dimensional($N = 2$), where $b(\overrightarrow{r'}, t)$ and $d\Omega$ are expressed by [27]:

$$b(\overrightarrow{r'}, t) = -2t \int_t^{\infty} \frac{d}{\sqrt{c_s^2 \tau^2 - d^2}} \frac{\partial}{\partial \tau} (\frac{p(r', \tau)}{\tau}), \qquad d\Omega = \frac{\mathrm{dC_0}}{d^2} \frac{\boldsymbol{\acute{n}_0}.\mathbf{d}}{d} \tag{18}$$

Here $\mathrm{C_0}$ is a line element on the detection curve, i.e. the curve along which the line sensor elements are distributed in a plane perpendicular to the line direction.

2.2.2.1.2 Radon Transform and its Inverse

The Radon transform generates a set of linear projections of an existing function for different angles. If we have a two dimensional function $f(x, y)$ and define angles θ, so that $0 < \theta < \pi$, the Radon transform of this function can be expressed with the following formula:

$$f(x, y) = \rho(s, \theta) =$$

$$\int_{-\infty}^{+\infty} \int_{-\infty}^{+\infty} f(x, y) \delta(x cos\theta + y sin\theta - s) dx dy = \int_{-\infty}^{+\infty} f(s cos\theta - l sin\theta, s sin\theta + l cos\theta) dl$$

(19)

Here $\rho(\theta, s)$ is the transformed function and is often referred to as sinogram, because every point in $f(x, y)$ creates a sinusoidal pattern in $\rho(s, \theta)$ after Radon transform. The principle of the Radon transform can be seen on Fig. 2. As we can see here the δ function transforms the two dimensional integral into a one dimensional line integral along the line $x cos\theta + y sin\theta = s$.

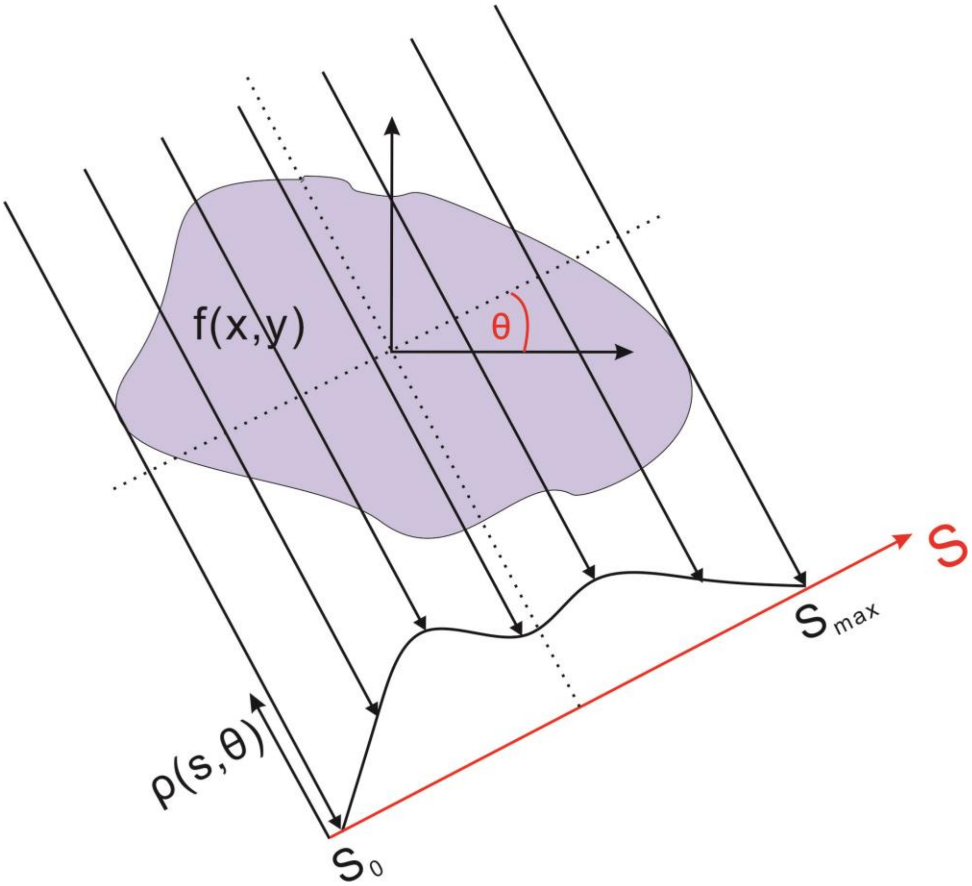

Figure 2. Representation of the Radon transform. For every rotational angle of the sample a set of projections is generated out of an existing function. In photoacoustic tomography the inverse Radon transform is used, which retrieves the underlying function from the projections.

In photoacoustic tomography, however, of more significant importance is the inverse Radon transform $R^{-1}\rho$, which is used to obtain the function $f(x,y)$ from an already known set of projections. One way of solving the inverse Radon transform is with the help of the so called Fourier slice theorem, which states that a 1D Fourier Transform of the projection $\rho(s,\theta)$ at angle θ is equal to the 2D Fourier Transform of $f(x,y)$ along a line at the angle θ.

In the case of PAT with line detectors we obtain a set of 2D back-projections for different orientations θ of the sample. For a certain plane perpendicular to the z-direction we use back-projection data and formula (19) to calculate $f(x,y)$ for this plane. By stacking all calculated functions $f(x,y)$ in the z-direction we finally acquire a 3 dimensional image, which is a representation of the initial pressure distribution.

2.2.2.2 Detector-array geometries

There are three types of detector geometries that are commonly used –cylindrical, spherical and planar. They can be seen on Fig. 3.

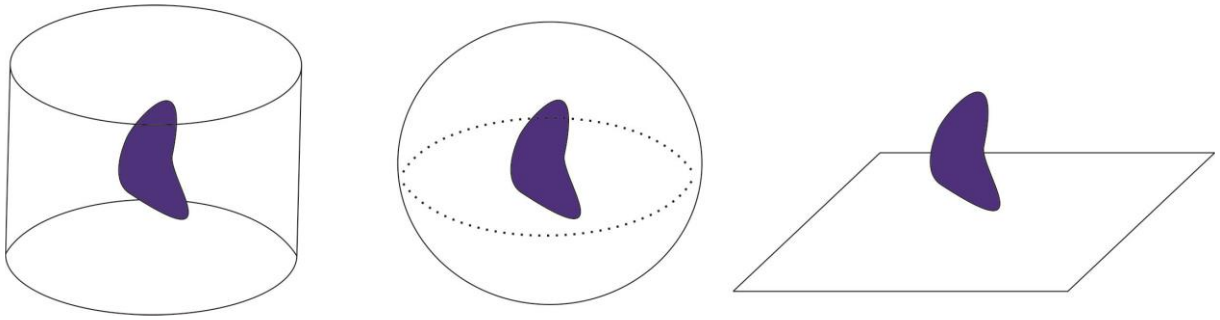

Figure.3 *Detector array geometries.*

Spherical PAT is a technique that can be implemented by the mechanical scanning of a sample with an arc-array transducer. By rotating the sample we get information about the whole sample volume. By merging the data collected by all transducer elements an image can be reconstructed. With such a system a high isotropic spatial resolution can be achieved within the imaging volume. Besides an arc-shaped array scanning around the sample [28] also a hemispherical array can be used, where the detectors are placed in a spiral pattern on a hemispherical surface as it was demonstrated for breast imaging [29].

In the case of a planar geometry the detection of ultrasonic waves can be done by either using a 2D array of piezoelectric transducers or optical interferometry [30,31,32]. In the latter case, an optical interrogation beam scans a planar etalon. Using an optical approach has several advantages. Firstly the optical sensor can be manufactured to be optically transparent, which eases illumination of the object. A second advantage is that it can achieve high spatial resolution, by using a highly focused interrogation beam and at the same time increasing the spatial sampling frequency, without affecting the sensitivity of the system. Thirdly the optical detector is also sensitive at low ultrasound frequencies, which enables studying the complex nature of photoacoustic sources, which naturally emit rather broad bandwidth sound waves. The interferometer based approach however is much slower compared to a system using a 2D piezoelectric transducer array [33] due to the requirement to scan a single detection point over the etalon.

A cylindrical PAT uses usually an ultrasonic transducer that is rotated around the sample. By scanning in a circle around the object, information about the pressure distribution data of a cross-section within the sample is recorded, which can later be reconstructed into an image by applying a back projection method. This kind of 2D imaging requires some kind of cylindrical lens that focuses the detector sensitivity into the chosen cross section. To increase the speed of the measurement a ring-shaped transducer array can be manufactured [34]. Compared to a spherical view system, which can be only used for 3D imaging, the cylindrical PAT can acquire 2D (image cross-sections) and 3D images (by scanning in the vertical direction with the ring transducer array). In this thesis a tomograph is introduced, where the data is collected by line sensors positioned on a half-cylindrical surface, leading to projection images of the initial pressure distribution. The array is described later in the experimental setup section.

2.3 Sensor types

In Photoacoustics two methods of pressure wave detection are used.

The first is by using an optical detection system. Examples for such optical sensing systems are the Fabry-Perot [35] or the Mach-Zehnder interferometers [30]. Polymer films can be adapted to behave like Fabry-Perot interferometers and are also commonly used in photoacoustics [32]. Some advantages of the optical sensors are that they can perform measurements at high spatial resolution, they can be built to be optically transparent (e.g. a laser beam in a Mach-Zehnder interferometer) and are not strongly influenced by electromagnetic waves.

The second type of acoustic wave detection is using piezoelectric sensors. The piezoelectric effect states that some materials have the ability to generate electrical charge if mechanical stress is applied. By applying a force ΔF a net dipole moment is created in the material, because of a displacement of the charged atoms, and it becomes electrically polarized. This effect is also known as the direct piezoelectric effect. The relationship between ΔF and the charge change ΔQ is linear and follows the equation $\Delta Q = d_{33}\Delta F$, where d_{33} depends on the material and is described as the specific piezoelectric constant. Piezoelectric media placed in an electric field are deformed. This is called the inverse piezoelectric effect.

When building piezoelectric sensors, usually piezoelectric material is deposited between two metallic layers, which act as electrodes. When the material is in a state where no mechanical force is applied, the sum of positive and negative charges in it is zero. Applying stress on the piezoelectric material leads to formation of dipoles, the crystal becomes polarized and thus a potential difference between the two metallic electrodes is formed.

Materials used to manufacture piezoelectric sensors can vary from piezoelectric crystals (Quarz, Turmalin) and piezoelectric ceramics (lead-zirconium-titanate) to materials based on polymers like Polyvinylidene Fluoride (PVDF). PVDF-films are a viable choice for the manufacture of sensors because of their high flexibility [36]. They can be easily cut into any desired shape and glued to almost any type of material. At high pressures they do not lose their piezoelectric properties like some piezoceramics [37] and can be produced at a lower cost [38].

Sensitivity of the piezoelectric sensors can be estimated using the signal to noise ratio. It is given by the relationship between the amplitude of the measured signal divided by the root-mean-square value of the noise.

$$SNR = \frac{S_{max}}{RMS_{noise}} \quad (20)$$

$$RMS_{noise} = \sqrt{\frac{\sum_{r=1}^{N} R_r^2}{N}} \quad (21)$$

Here R_r is the noise value at position r and N is the number of position values taken. To get a measure of the sensitivity, noise equivalent pressure can be introduced as the pressure signal for SNR = 1. Given the absolute pressure amplitude p_{max} of the signal originating from the source and the SNR, NEP can be written as:

$$NEP = \frac{p_{max}}{SNR} \quad (22)$$

In the case of point like detectors the received signal can be expressed by integration of the initial pressure over the surface of a sphere where the detector is assumed to be a point in its center (Eq. 15). In reality detectors are not points but have a finite size and this limits the spatial resolution of the reconstructed image. If the object is placed in the acoustic near field of the detector or in the transition region, the final image will appear blurred.

The issue with the finite size of detectors can be solved by using large area integrating detectors [Lit. E.g. Haltmeier et al.]. The measured signal here is a projection over a plane and is given by the integral of the distribution of energy density over the detector area, assuming that the detector has a size much larger than the imaged object and the object itself is placed in the near field of the detector. The integrating behavior of the detector can be taken into account in the reconstruction. As long as the near field condition is satisfied, this can be shown to result in an exact reconstruction. Acquisition of a three-dimensional image requires measurements from all sides of the sample resulting either in a complicated motion of the detector or the object.

This is why we focus on piezoelectric line sensors. Integrating line detectors can be viewed as a combination of point and planar detectors. For the two-step reconstruction algorithm outlined in 2.2.2.1 to be applicable, the lines have to have infinite length. However, in practice the lines have to be sufficiently longer than the imaging object, as shown in Fig. 4.

A problem when implementing a transducer array is limited view, because in practice the sample can be accessed from only a limited range of angles, which results in an open scanning curve S_0. This leads to artefacts in the reconstructed image, due to missing high-frequency information for some object boundaries. For an array with an open scanning curve it can be shown that data for a stable reconstruction of all points of an object can be collected [39] if the detection view angle, as seen in Fig. 10, is larger than π or 2π for 2D or 3D reconstruction, respectively [27].

A minimum requirement exists for the size of the detector when imaging with planar or line transducers in order to satisfy the near field condition. An object inside a ball with radius R (Fig. 4.) is to be measured with a detector that touches the ball. Waves propagating perpendicularly to the detector should arrive earlier than any wave can reach the end of the line. This leads to the condition that the detector having the form of a disc or a line should have a diameter or length of at least $2R\sqrt{8}$ [40].

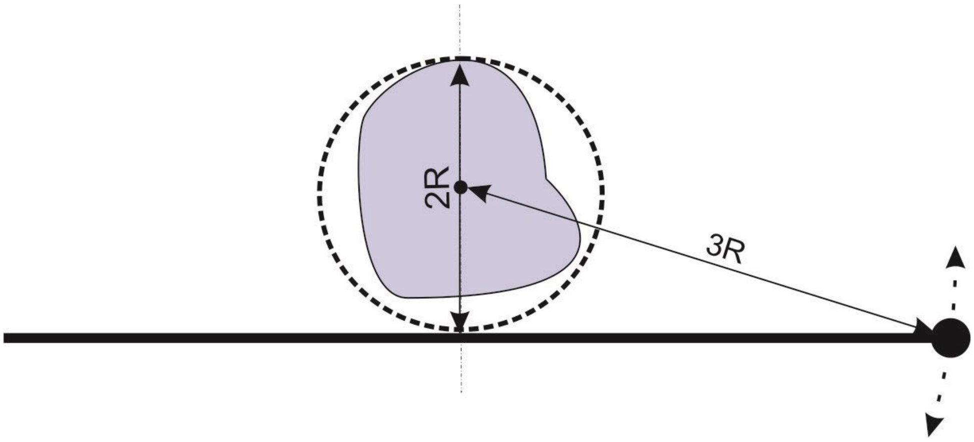

Figure 4. Requirement for the size of photoacoustic line or planar detectors. If a sphere with radius R encloses the sample, the length or diameter of a linear or disc like detector should be at least $2R\sqrt{8}$.

In this thesis an array consisting of piezoelectric line sensors is used and further characterized.

2.4 Sound wave propagation in different media

In photoacoustics usually sound waves need to travel through different media in order to reach the detector. Between sample and detector there is usually water, in which the pressure wave travels differently compared to air. In this chapter the influence of different media on the acoustic wave will be described.

2.4.1 Speed of sound

It is important to mention that the speed of sound can change drastically, depending on what type of material it is travelling through. In solids the factors that influence the speed of sound are elastic properties of the material and its density. Sound travels faster through solids with high elastic moduli. In fluids the sound waves are dependent on the density and compressibility of the given fluid. In gasses the speed of sound strongly depends on the temperature and the density. Here an increase in temperature causes the molecules in the gas to move faster which contributes to the speed of sound and increases its speed. Also in liquids like water the speed of sound increases with temperature.

The speed of sound can be calculated by:

$$c = \sqrt{\frac{K}{\rho}} = \sqrt{\frac{1}{\chi \rho}} \tag{23}$$

Here ρ is the density of the material, through which the wave is travelling and K is the bulk modulus. For fluids the inverse quantity of K is used, called the compressibility χ. These two values are used to describe the variation of volume V or density ρ by variation of the pressure.

$$K = \frac{1}{\chi} = \left[-\frac{1}{V}\frac{\partial V}{\partial P}\right]^{-1} = \left[\frac{1}{\rho}\frac{\partial \rho}{\partial P}\right]^{-1} \tag{24}$$

The next table shows the speed of sound in m/s for some known materials:

Table 1. Speed of sound for some known materials

Material	**Speed of sound[m/s]**	**Material**	**Speed of sound[m/s]**	**Material**	**Speed of sound[m/s]**
Air	343	Fat	1450	Blood	1550
Water	1490	Myocardium	1550	Liver	1570

2.4.2 Frequency, wavelength and attenuation

Acoustic signals can be described as vibrations, characterized by their frequency f (vibration per second) or by the period T (duration of the vibration), where the link between them is:

$$f = \frac{1}{T} \tag{25}$$

Wavelength of the acoustic wave can be described as the distance between two points in the medium, where the same vibrations take place with delay T, or 2π phase shift [41]. In other words, this is the distance the wave travels with velocity c in a time T. This is expressed by:

$$\lambda = cT = \frac{c}{f} \tag{26}$$

A few limitations apply to the frequencies of sound waves [41]. When propagating in water they experience frequency dependent attenuation, thus limiting the maximal frequency range of the signals that are to be measured. In photoacoustics the samples are usually placed in a water bath for better coupling in order to avoid pressure loss. The attenuation coefficient $\alpha(\omega) = \alpha_0 \omega^\eta$ can be used to describe the attenuation in the following way:

$$p(x + \Delta x, \omega) = p(x, \omega) e^{-\alpha(\omega)\Delta x} \tag{27}$$

ω here is the angular frequency, p is the pressure, Δx is the wave propagation distance and α_0 and η are real positive parameters depending on the material, which are obtained by fitting of experimental data. η can take values from 0 to 2. For example acoustic attenuation in water, many metals and crystalline materials are always frequency-squared dependent, in this case $\eta = 2$.

2.5 Acoustic waves at interfaces

Every medium has a specific acoustic impedance Z. It describes how resistant the medium is for pressure waves propagating within it and is given as the ratio between applied pressure and resulting particle velocity. The acoustic impedance can be expressed by the product of the density and the speed of sound.

$$Z = c_s \rho \tag{28}$$

Acoustic waves at interfaces experience reflection. How much of the wave is transmitted depends on the difference in impedances of different media.

In this thesis we have a transition from liquid to solid (PVDF) with different acoustic impedances Z_1 and Z_2 before the signal can be registered. The acoustic wave arrives at the interface at an incident angle of 90°. The amount of transferred acoustic pressure can be described by the transmission coefficient, which depends on the impedances of the two media:

$$d_T = \frac{2Z_2}{Z_1 + Z_2} \tag{29}$$

The relationship between transmitted and incident pressure wave amplitudes p_T and p_I can then be expressed by:

$$p_T = d_T p_I \tag{30}$$

Calculation of d_T in the case of a water/PVDF interface yields a value of 1.44, which means that the pressure amplitude is one and a half times higher in PVDF.

Due to the discontinuity at the water – PVDF interface, a part of the pressure wave is reflected. The reflected fraction of the incident pressure can be calculated by multiplying the amplitude of the incident wave with the reflection coefficient $d_R = \frac{Z_2 - Z_1}{Z_1 + Z_2}$.

2.6 Signal Processing

What the ultrasonic transducer detects as an input signal can be described in the following way:

$$U_{in}(t) = S(t) + S_{noise} \tag{31}$$

Here $S(t)$ is the photoacoustic signal that has reached the sensor with a particular noise level S_{noise}, which depends on the thermal noise and on the experimental setup. To describe the output signal, $U_{in}(t)$ is convolved with the temporal response function $H(t)$ of the transducer:

$$U_{out}(t) = U_{in}(t) * H(t) \tag{32}$$

Here, "$*$" denotes convolution. To obtain the real signal, $U_{in}(t)$, the measured output has to be deconvolved with $H(t)$. A way to determine the impulse response function is to measure the signal originating from a known source. $U_{in}(t)$ for this source can be simulated and an estimate for $H(t)$ can be found by deconvolution. The downside to this deconvolution technique is the increase in noise, which in our case has to be minimized in order to get better quality images.

To minimize the noise a band pass filter is embedded in the reconstruction algorithm (Fig. 5.). It can be used also to eliminate low-frequency fluctuations in the detected signals, which may give rise to artefacts in the back-projected images. A disadvantage is that it sometimes filters part of the real signal at higher frequencies and thus may reduce the achievable resolution.

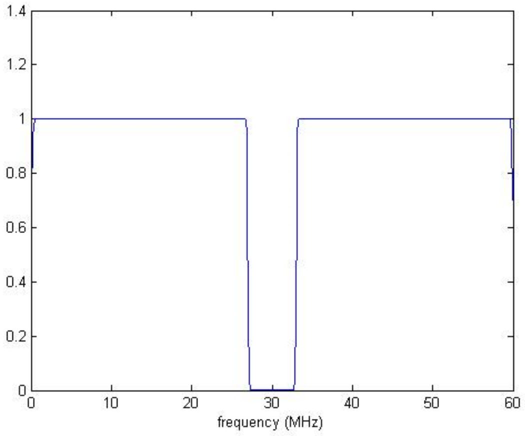

Figure 5. Band pass filter used during the reconstruction process. Its low and high frequency limits are 300 kHz and 27 MHz, respectively.

After applying the reconstruction algorithms, mentioned in section 2.3.2.1., we generate a three dimentional matrix with values of the amplitude of the energy density or the initial pressure. A way to display the 3D image is to generate a two dimensional maximum amplitude projection (MAP) for a predefined orientation of the sample. To generate a MAP in a specific direction means to look for the highest amplitudes of the reconstructed data array and project them on a 2D plane perpendicular to this direction. This results in a 2D image, where a good overall impression of the sample can be obtained. To study details of the reconstruction or to make comparisons between reconstructed images, it is sometimes better to generate section images, i.e. amplitude values in a defined plane within the 3D data volume.

The back-projection data can be manipulated in a way to rotate a desired back-projection image at a certain angle about the z-axis (the rotation axis used in the data acquisition). This process is used when comparing two pictures of a sample, where one of them started at a different initial orientation before data acquisition. This is done before applying the inverse Radon transform by using a cross correlation. The data of the two compared images is stored in two different matrices containing back projection data as a function of distance from the rotation axis and rotation angle (the sinogram). After plotting the cross correlation the direction and the number of the columns that need to be shifted in one sinogram in order to obtain the desired rotation after applying the inverse Radon transform can be determined. Fig. 6 shows how this method works step by step. The sample used here is described later in section 4.1.3.

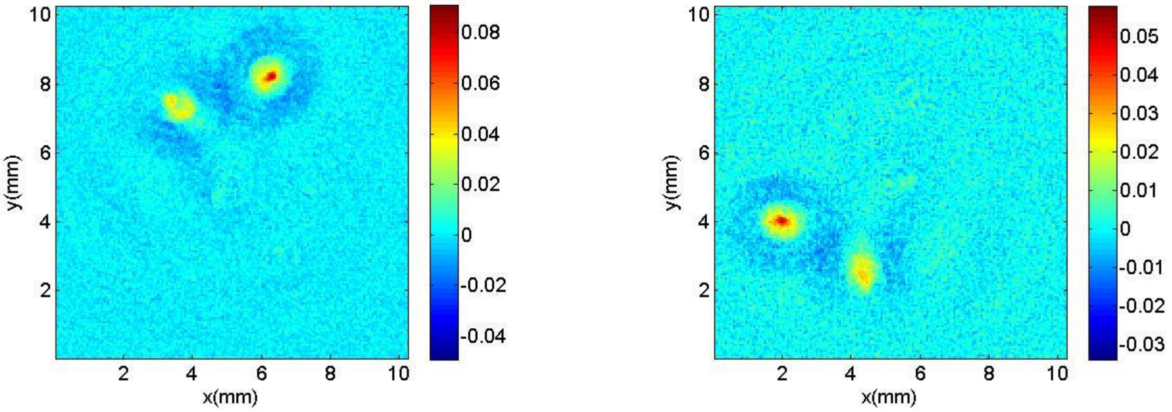

(a)

(b)

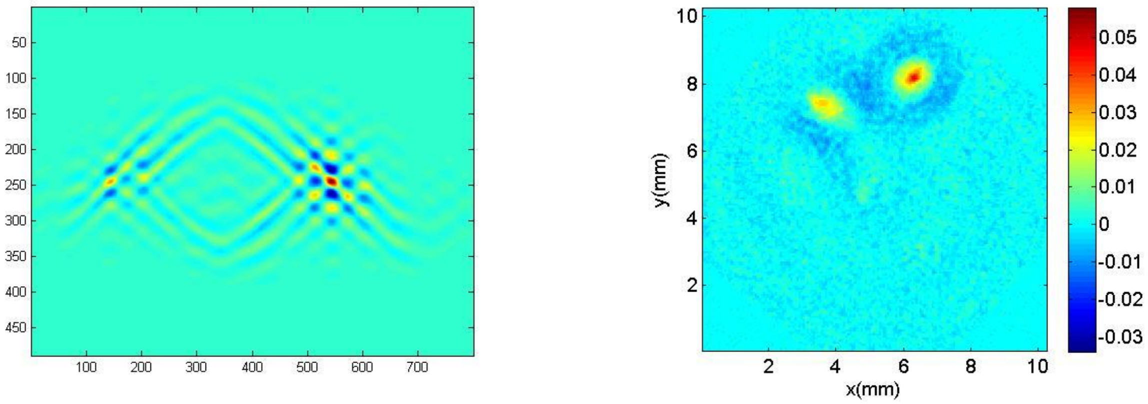

(c) (d)

Figure 6. Slices of two small tubes, filled with highly absorbing liquid. On a) a slice through the sample perpendicular to the z-direction can be seen. b) shows the same slice measured at a different wavelength, where it appears to be rotated, compared to a). A cross correlation between the sinograms used to create a) and b) can be seen in c). It helps us to manipulate the back-projection data in a way, so that we can rotate the image in a desired direction by a defined angle. In d) the rotated image from b) is seen, with an orientation similar to image a).

3 EXPERIMENTAL SETUP

3.1 Schematics

Fig. 7 shows the experimental setup.

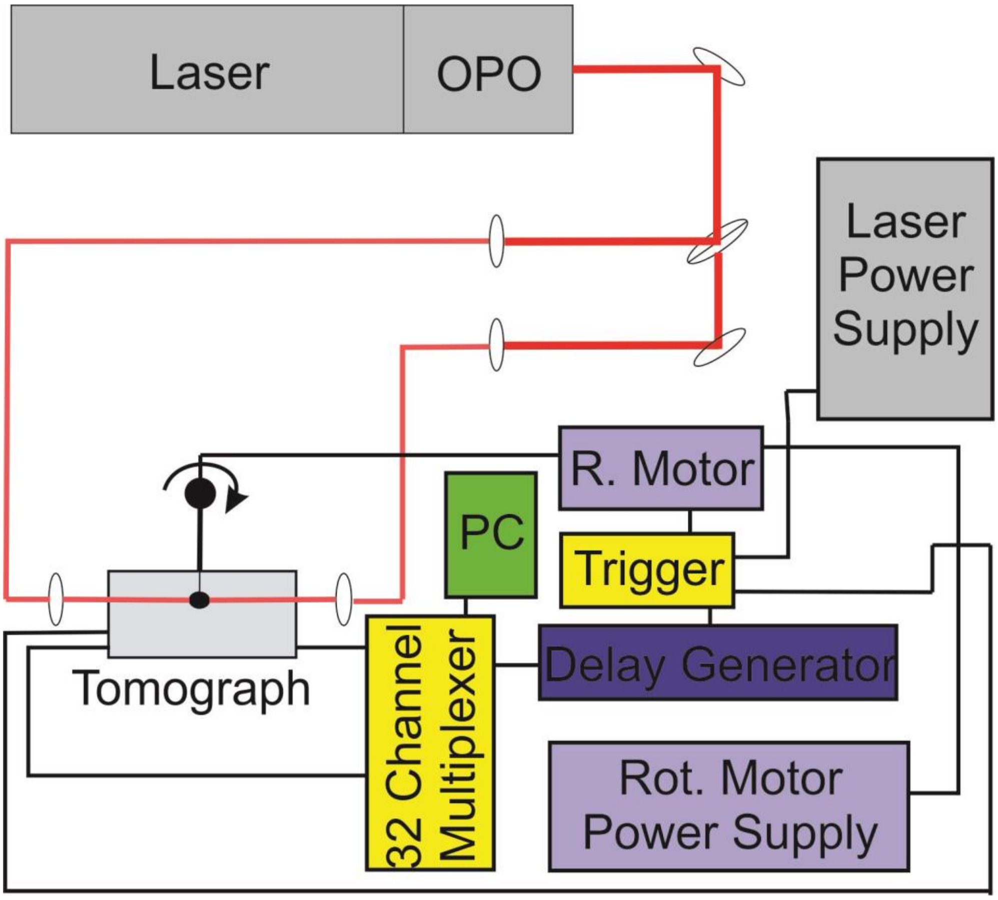

Figure 7. A schematic representation of the used experimental setup.

Here a laser pumps up an OPO, where the desired wavelength can be chosen in the visible or the infrared region of the light spectrum, depending on the pump wavelength. Then the beam is split in two by a beam splitter and then focused into two optical fibers. The sample is submerged in a water bath for better coupling and is illuminated from both sides by the light coming from the end of optical fibers. More detailed information will be presented further in the next sections.

3.2 Laser

Two types of lasers were used in this experimental setup. The first one is a Nd: YAG laser (Continuum Surelite), which pumps an optical parametric oscillator (OPO) at 355nm. It generates 6 ns horizontally polarized pulses at a repetition rate of 10Hz. The pump energy can be adjusted by changing the Q-switch delay, which is the time between the firing of the flash lamp and the opening of the Pockels cell. The relationship between pump energy and Q-switch delay is shown in the next table:

Table 2. Relationship between Q-switch delay and laser output energy

Q-switch Delay [μs]	**E[mJ]**	**Q-switch Delay [μs]**	**E[mJ]**
370	1	240	85
300	24	230	99
280	32	220	112
270	42	210	119
260	52	200	122
250	1	170	147

During acquisition of experimental data, the pump energy was set to ~100mJ, which yielded a value of ~20mJ for the energy measured after the OPO at 540nm. The OPO output wavelength is tuned by rotating the beta barium borate (BBO) crystal within the OPO cavity, thereby changing the phase matching condition. The motorized rotation stage was calibrated with a spectrometer.

The second laser used was an Innolas Spitlight 600 OPO laser that has an output of 532nm and a repetition rate of 20Hz. The OPO, which is positioned in the same housing, can be tuned to wavelengths in the near infrared and infrared regions of the light spectrum varying from 650-2500nm. The signal output energy after the OPO can go up to 100mJ. Signals from samples were acquired at 750nm, where we measure an output energy of 97mJ after the OPO at 60% laser power.

3.3 Illumination

The laser pulses go through a beam splitter that separates the light beam into two separate parts, which are focused onto two optical fibers with diameter of about 1mm by two convex lenses with focal length f = 80mm. The distal fiber ends are mounted on the two sides of the tomograph, and the fiber exit was imaged into the center of the water bath by two f = 25mm lenses. The distance between the fibers and the lenses is chosen in a way that we get a spot with 8mm diameter. The output energy of each of the fibers is measured to be 4,5mJ and 5,2mJ in the case of the continuum laser at 540nm, and about 20mJ and 12mJ in the case of the Innolas laser at 750nm. Calculating the radiant exposure gives us values of about ~9 and ~10mJ/cm^2 in the first case and ~40 and ~25mJ/cm^2 in the second case. From the energy measured before the coupling lenses and after each fiber a transmission of 57% was determined. The attenuation is due to coupling and reflection losses and attenuation inside the fibers.

3.4 Ultrasound-array

3.4.1 Sensor design

The size of the 64 line sensors was chosen according to the sample size. The length of an ideal line sensor should be infinite, since it is the length over which the pressure signals originating from the specimen have to be integrated in order to achieve a pure two-dimensional signal. In reality it is enough for acoustic waves coming from every point of the sample to reach the sensor before any wave can reach the end of the line, as it was illustrated in Fig.4. For an object that can be confined in a sphere with radius r that does not touch the detector line a slightly smaller length L can be chosen than the value of $2R\sqrt{8}$ found above. It can then be calculated according to Fig.(8) by the following formula:

$$L = 4\sqrt{r^2 + rR} \qquad (33)$$

Here r is the radius of a sphere that completely encloses the examined sample and R is the distance between sensor and the center of the sphere. For imaging small animals it is convenient to take $r = 20mm$ and $R = 50mm$, which yields a length for every line sensor of about $L = 150mm$. The width is chosen to be $1{,}5mm$. The line sensors are placed on a concave cylindrical surface with radius R at a distance $2{,}454\ mm$ from each other, leading to an angle between them of 2,8°.

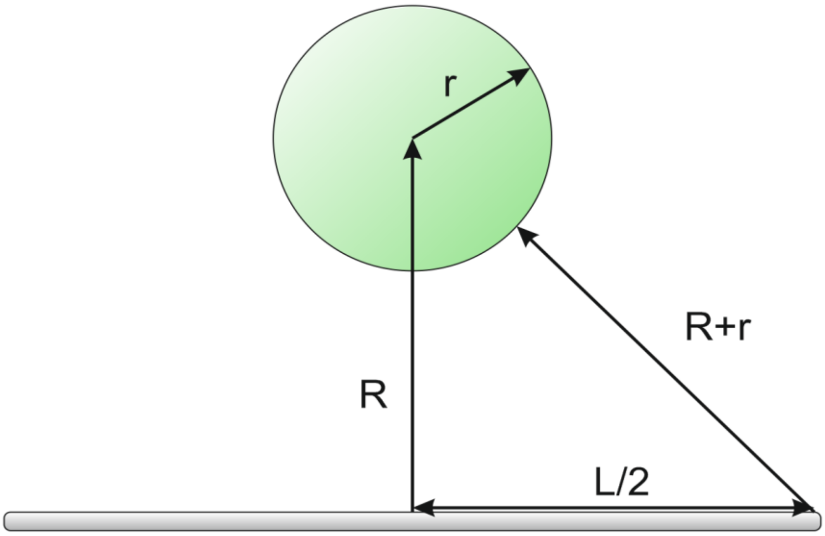

Figure 8. Length of the line sensor, which depends on the sample size

3.4.2 Array manufacturing [42]

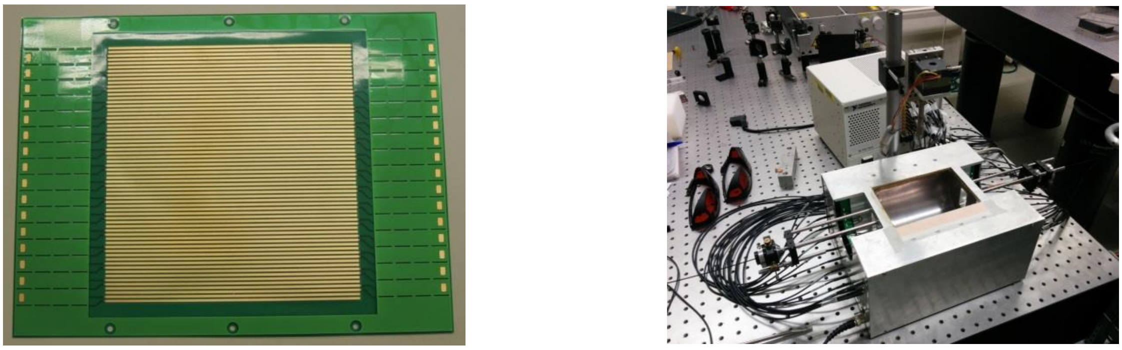

(a) (b)

Figure 9. a) Circuit board used for the construction of the tomograph. In the middle 64 copper lines can be seen, used later for the formation of the electrodes. On b) the already constructed device is displayed.

As a base for the construction of the array a flexible circuit board made of FR 4 with a 35µm thick copper layer, forming 64 line shaped electrodes, was glued to PVC block with a concave cylindrical opening yielding the desired array radius of 50 mm. An aluminium housing was used for electric shielding of the entire device. For the formation of the sensing elements an 110µm PVDF film, metalized on one side, was cut in the desired shape and then glued onto the base. Amplification of the signal is done in two stages: 64 pre-amplifiers are used in the first stage to amplify the signal from the electrodes, which are multiplexed to 32 amplifiers in the second, yielding a $59{,}5 dB$ total gain in the frequency region $80kHz - 40MHz$(Fig. 10.). To acquire data a 32 channel analog-digital converter was used (sect. 3.3).

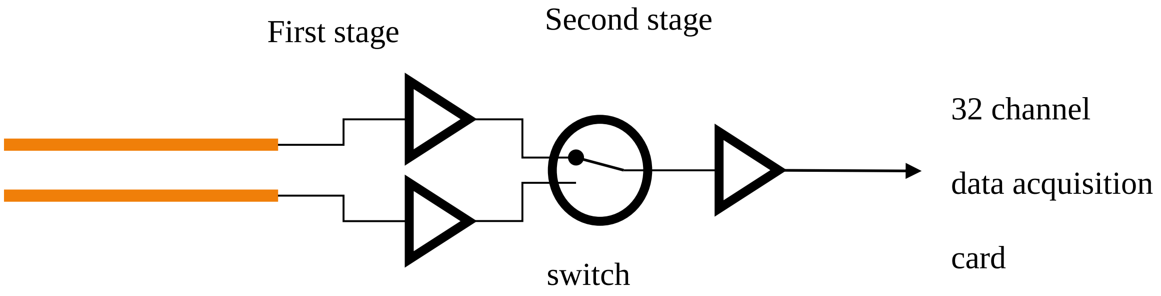

Figure 10. Amplification and multiplexing of the measured signal

For a complete volumetric scan, the sample in the water bath needs to be rotated about an axis perpendicular to the line direction. The shape of the array is purposely chosen to form a water tank. To overcome the limited view problem, the sample needs to be submerged in the water tank as shown on Fig. 11. In this way sufficient information can be acquired to reconstruct a three dimensional image.

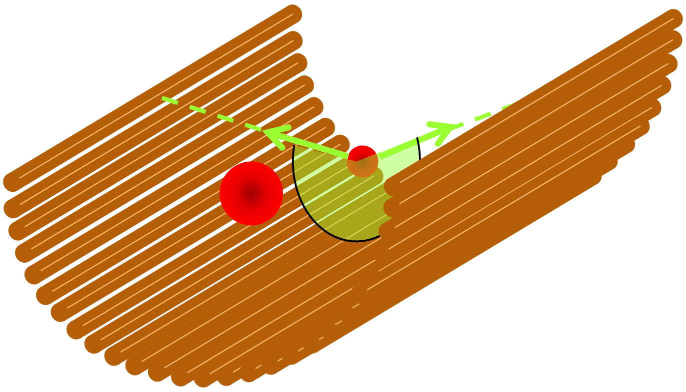

Figure 11. How the sample should be positioned in order to overcome the limited view problem. The angle indicated in green should be larger than 180°.

3.5 Multichannel Data Acquisition Device

The amplified and multiplexed signal, measured by the detector array, is fed into a 32 channel device. Data acquisition as mentioned above is done by 4 analog-digital converter cards (National Instruments PXI-5105). Each of these cards has 8 simultaneously sampled channels, 12-bit vertical resolution and a real-time sampling rate of $60MS/s$. The cards convert the signal and transfer it to the PC, where it can be visualized in real-time.

3.6 Measurement Control

The program used here to control measurements is Labview. A special code has been written, where the number of pulses to be measured and signal averaging can be chosen. Choosing an averaging factor of 4 for example means that the signal detected by every sensor will be an average out of the waves generated by 4 laser pulses. After that the sample will be rotated by a small angle of 0.9° and the process will be repeated. By selecting the number of pulses and the averaging rate we determine the total angle of rotation of the rotary stage. For example, by choosing 3200 pulses with four times averaging, the sample will be rotated in the full 360° around its axis. The image acquisition time depends also on the pulse repetition rate and can be calculated by:

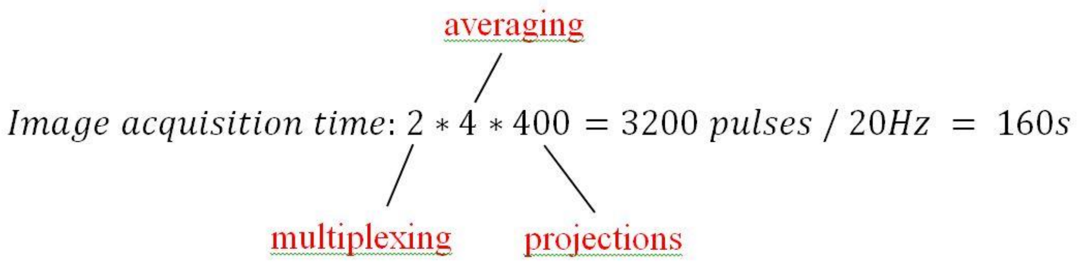

$$Image\ acquisition\ time: \underbrace{2}_{\text{multiplexing}} * \overset{\text{averaging}}{4} * \underbrace{400}_{\text{projections}} = 3200\ pulses\ /\ 20Hz\ =\ 160s$$

Figure 12. Image acquisition time

For each ultrasonic transducer the measured signal and the averaged one can be visualized in real time. To start a measurement we first have to open the valve for external water supply and start the water pump in the laser in order to keep the internal cooling water in the laser at a constant temperature of about 25°C. We have to make sure that the delay generator, the multichannel data acquisition device, the power supply for the rotational motor and tomograph, and the average and multiplex control box are switched on. It is important that the trigger switch on this control box is on the ‘off’-position before starting a measurement. We can then turn on our PC and start our control program. After adjusting the averaging rate and the number of laser pulses, we can switch on the laser pump source, open the shutter and then start our program. Hearing four clicks from the data acquisition device means that the analog-digital converter cards are working properly and prepared for recording data. The measurement starts when the switch on the control box is put in the ‘on’-

position. After the data acquisition has finished, it is important to measure the temperature of the water bath in the tomograph, as this value is needed later for image reconstruction.

4 EXPERIMENTAL PART

To evaluate the performance of the tomograph, several experiments for its characterization were carried out. The results of the characterization measurements were also used for optimization of the device.

4.1 Characterisation

4.1.1 Bandwidth

For the theoretical characterization of the bandwidth we used equation (32) to calculate the output signal $U_{out}(t)$ originating from a highly absorbing spherical source, which generates a known input signal $U_{in}(t)$. The latter was calculated for a sphere with radius 50µm, irradiated in direction of the line detector. This gives a uniform disc as 2D initial pressure distribution with the same radius. By taking the Fourier transform of $U_{in}(t)$ we obtain the detected signal in the frequency domain (Fig. 13.)

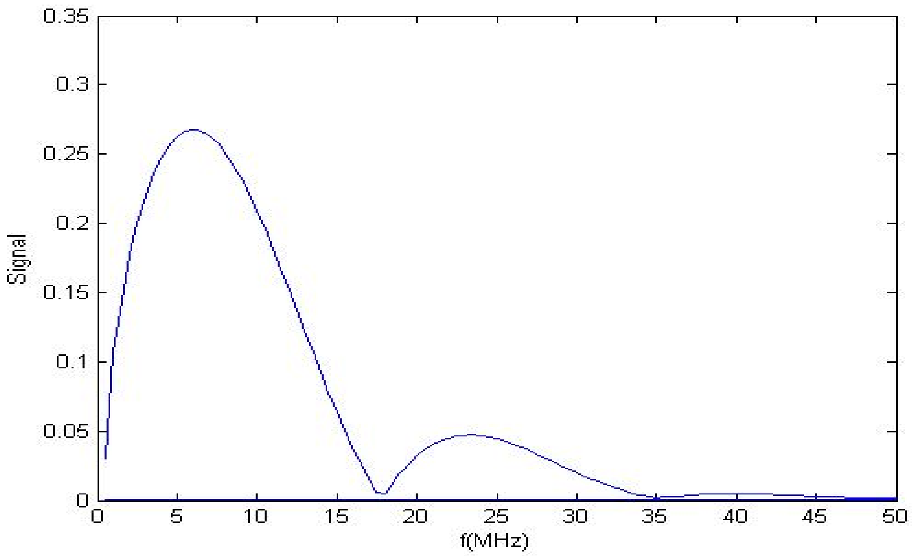

Figure 13. Theoretically calculated spectrum of a photoacoustic signal from a uniform disc

For the calculation of the impulse response function H we used a model, proposed by B. Cox [43], which is used to simulate the directivity function of a polymer film ultrasound sensor consisting of several layers. The result of this model is the signal amplitude as a function of frequency and incident angle of incoming pressure waves. In our case only normal incidence has to be taken into account, since the object is always located near the centre of the half circular array. Therefore, we have pressure waves coming at 0° incident angle from water into a system consisting of a PVDF film, which is glued to a copper electrode, which is in turn fixed on a substrate material. All of these materials have specific material constants, which were taken into account in the model. A graphical representation of the four-layer system is presented in Fig. 14 a):

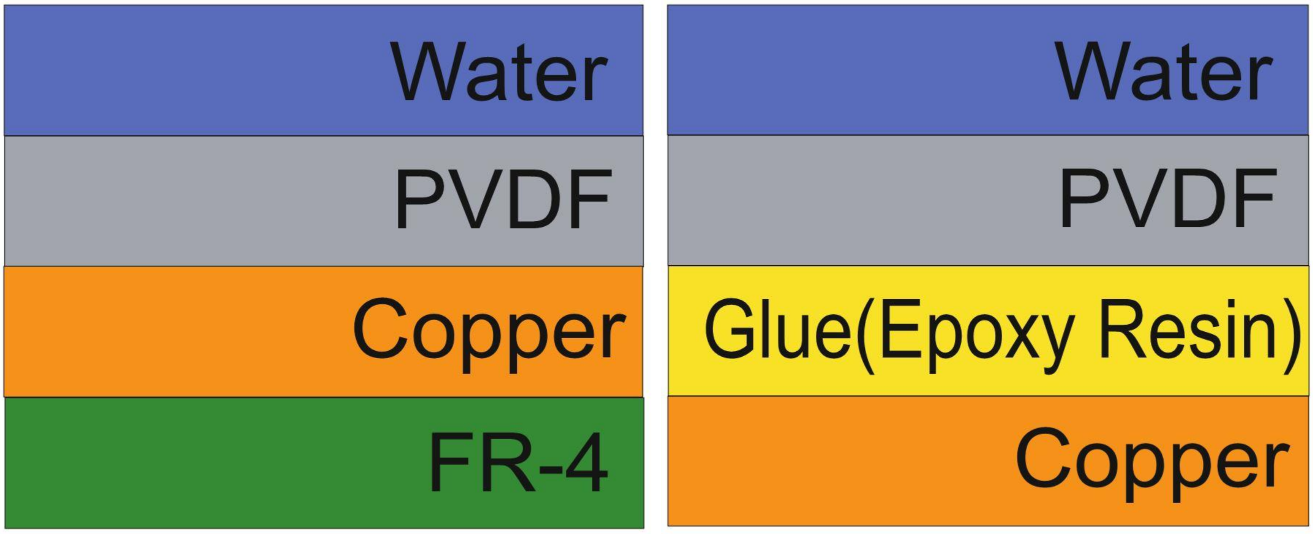

(a) (b)

Figure 14. Sensor 4-layer-system. a) sound waves travel through water, go through the PVDF layer, where part of the wave is reflected and another part reaches the copper layer. Reflection takes place at the copper-substrate interface as well. b) 4-layer-system, where we introduced a 10µm thick glue layer, formed by gluing the PVDF film onto the copper electrodes.

As a result, for the impulse response function of a 110µm PVDF film, placed on top of a 35µm thick copper layer, which is glued to a FR-4 substrate we get the spectrum shown in Fig. 15.:

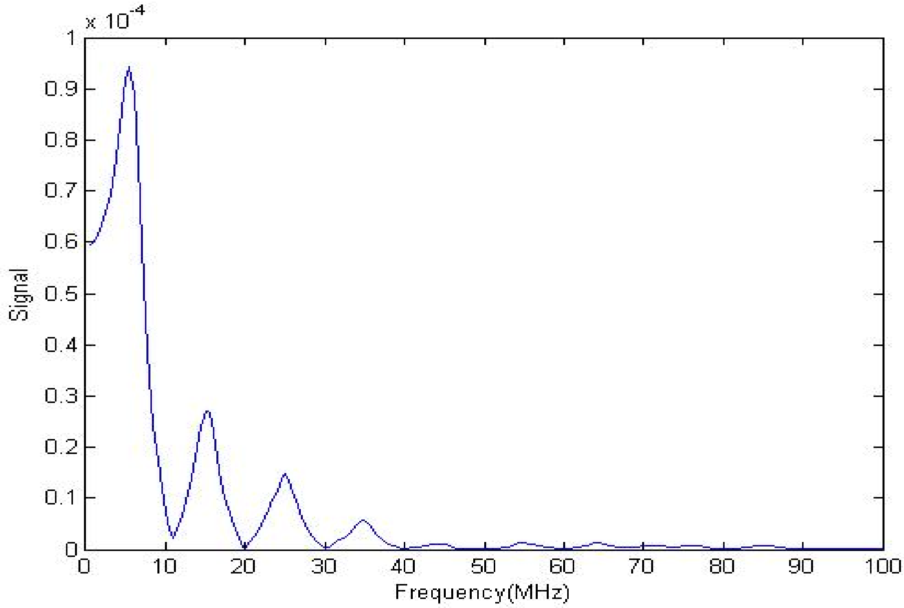

Figure 15. Impulse response function of the 4-layer-system presented in Fig. 14. a)

Multiplying both spectra, we obtain a representation of the frequency dependent output signal $U_{out}(f)$.

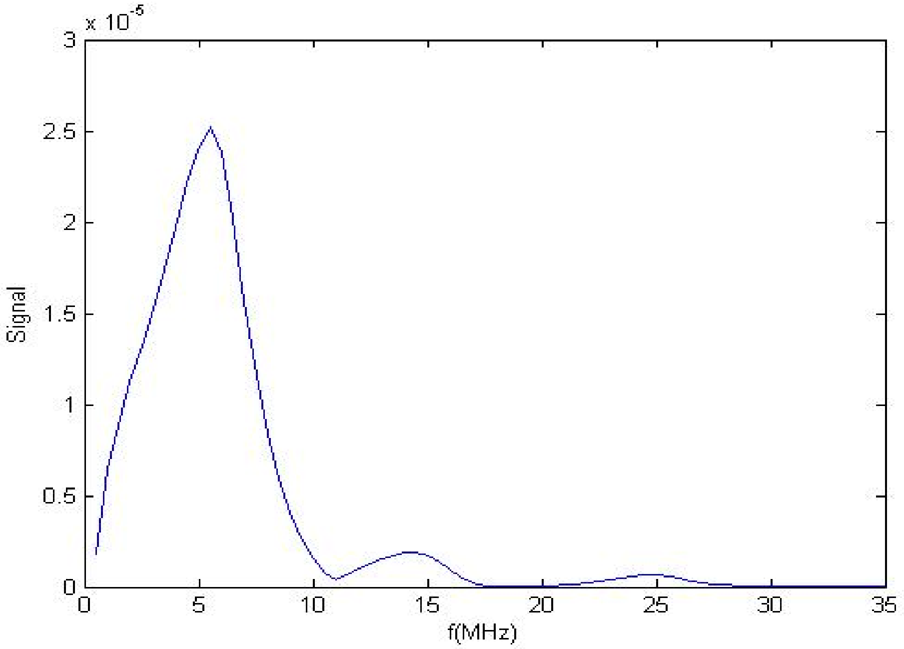

Figure 16. Theoretically calculated output of a sensor. Source is a 100μm diameter sphere. The calculation was done by multiplying the impulse response function with the calculated spectrum of the signal from a disc shaped source.

For the experimental characterization of the bandwidth of the device a microsphere with a diameter of about 100µm was used as a source. The spectrum of the measured signal can be seen in Fig. 17.

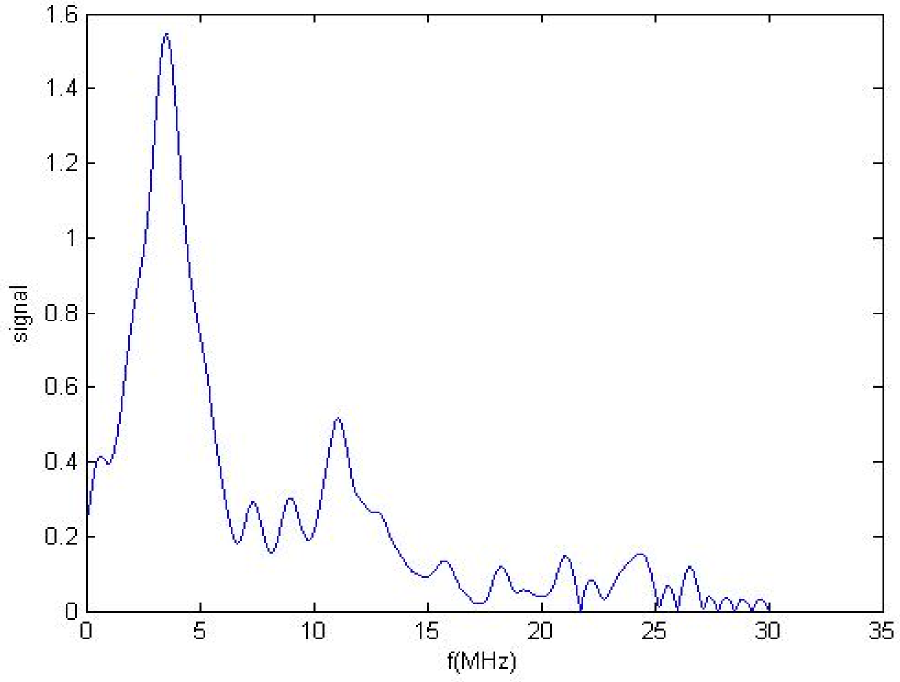

Figure 17. Experimentally measured spectrum of a signal generated by a microsphere with 100µm diameter.

From this it can be seen that in our theoretical calculation the main peaks at about 5 and 14 MHz appear shifted compared to the experimental result. An assumption is that the glue layer between the PVDF film and the copper surface has to be considered in the simulation. It delays the reflected wave from the copper electrode, causing the observed shift.

The model used here is a 4-layer system and it would be a difficult task to add one more layer, so we tried to see what influence it will have if the substrate layer is omitted. On Fig. 18 a comparison between the signal of our system with the substrate material (blue) below the copper electrode as in Fig. 14a and without the substrate material (red) but with an extended copper layer is illustrated:

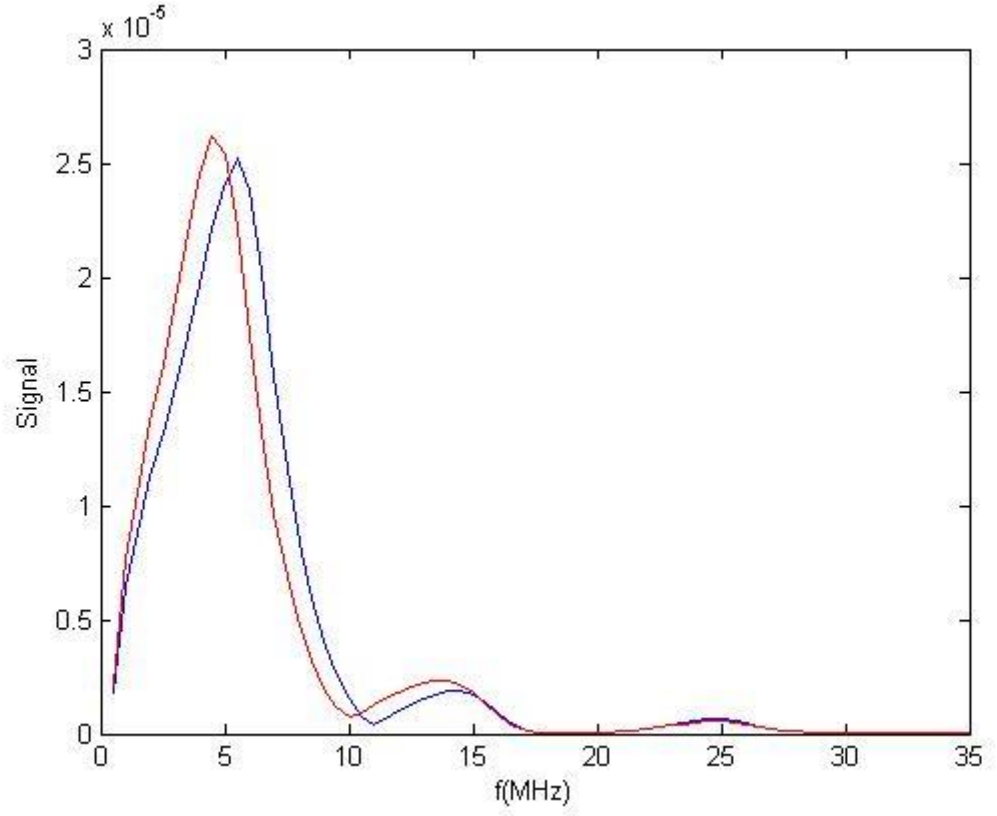

Figure 18, Influence of the substrate material. The blue curve represents a 4-layer system as seen on Fig. 14, a. The red curve shows the calculated result for the same layer system, but without the substrate layer.

The shift that the peaks have experienced is very small, which leads to the interpretation that the influence of the substrate material is insignificant and can be neglected. In this way by getting rid of the substrate layer we had the possibility to add a layer representing glue (Figure14 b) between PVDF and copper in our 4-layer model and investigate its influence on the received signal.

The added layer was assumed to have a thickness of about 10µm. We assumed that the glue has a sound speed similar to the PVDF film, but with a density typical for epoxy resin materials of $1150\ kg/m^3$. We calculated once more the impulse response function (Figure 19. a)) for this system and multiplied it with the theoretically calculated spectrum of the disc. As a result, we obtain the corrected spectrum, seen on Fig. 19 b).

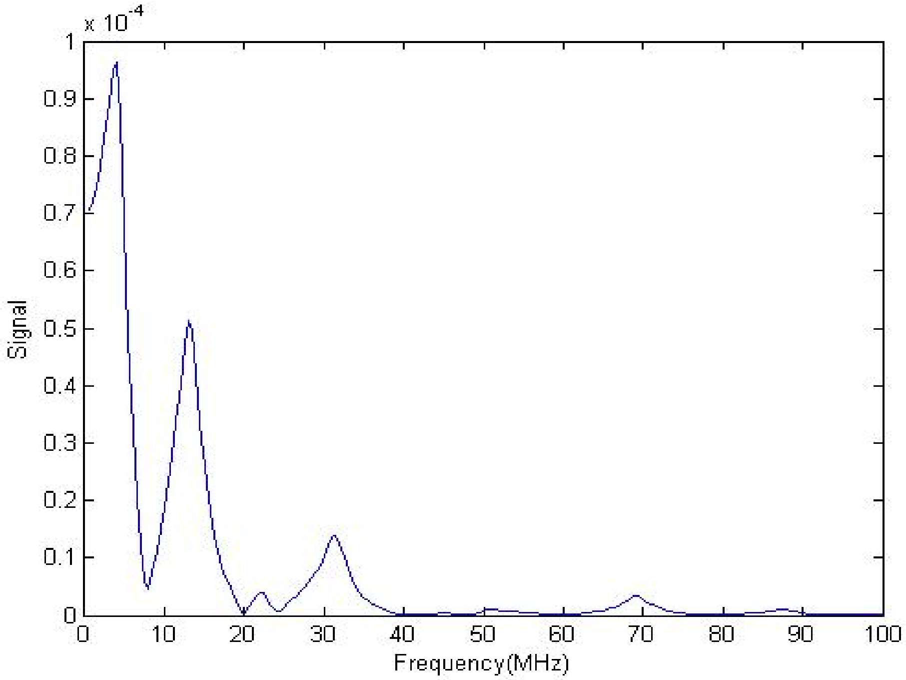

(a)

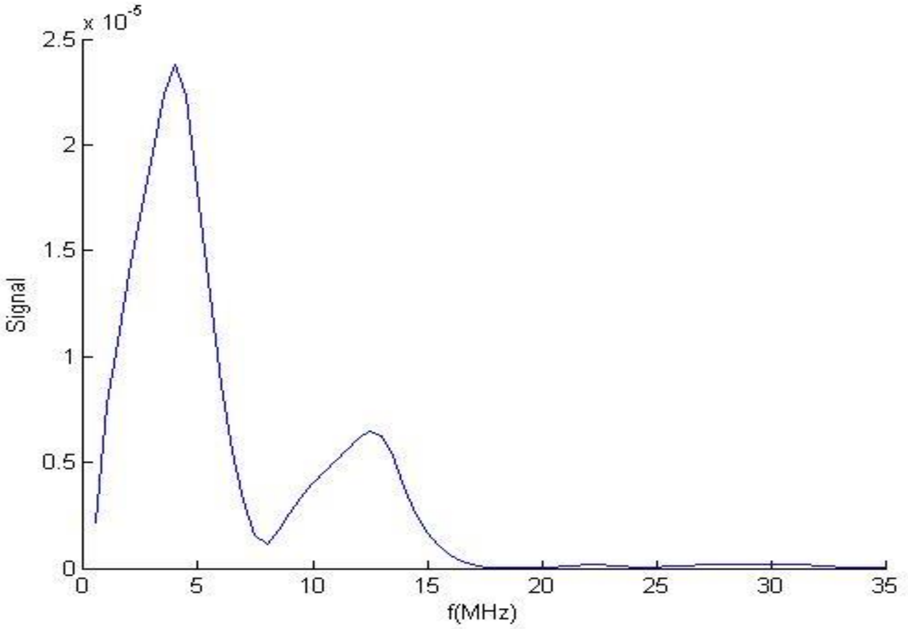

(b)

Figure 19. a) Impulse response function of the model, represented in Figure 12. b), b) Theoretically calculated output signal of the 4-layer-model consisting of water, PVDF, glue and copper.

A comparison of the results of our theoretical model and the experimental data is visualized in Figure 20:

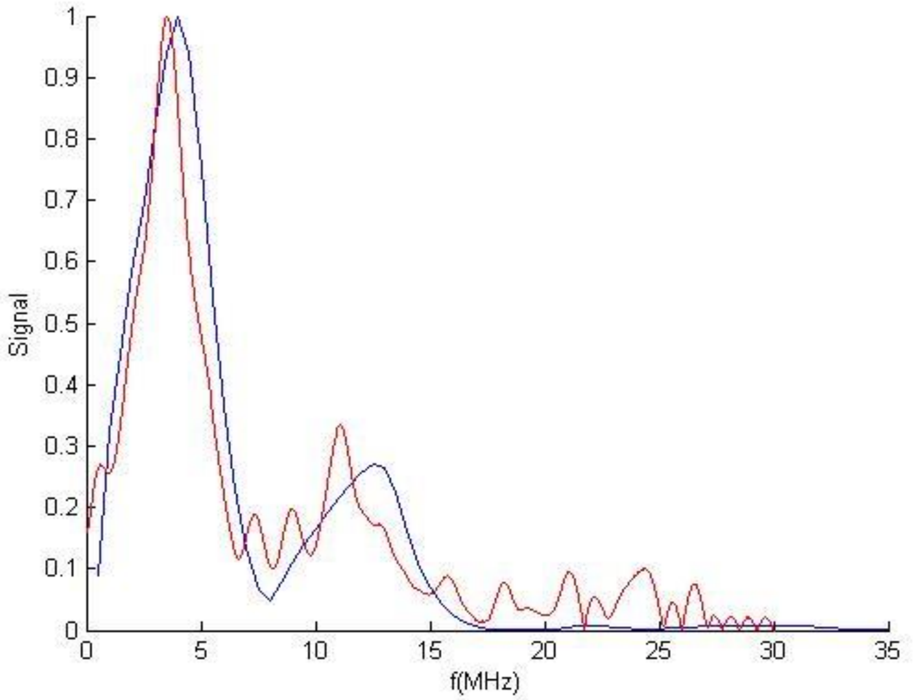

Figure 20. Comparison between the theoretically calculated signal for a microsphere (blue), with a size of 100μm, and the experimentally measured data (red).

From Fig. 20 we can make the conclusion that our theoretical model agrees reasonably with the experimental data. In particular, the peaks of the spectrum are approximately at the right position. It is important to mention that the formed glue layer between the piezoelectric film and the conducting material has a significant influence on the reflection of the sound waves in the system, which is also the reason why the peaks shift to lower frequencies.

Sound waves, as mentioned earlier, experience also frequency dependent attenuation when travelling through water. Using formula (27) we can calculate the transmission of a path length of Δx for each frequency. For the tomograph, the path length is about 50 mm from each sensor, leading to the frequency dependent transmission through water, as shown in Fig. 21a). To complete the model of the transfer function outlined above, this attenuation should also be taken into account in the calculation of the input signal. However, Fig. 21 b) shows that the influence of attenuation is rather small.

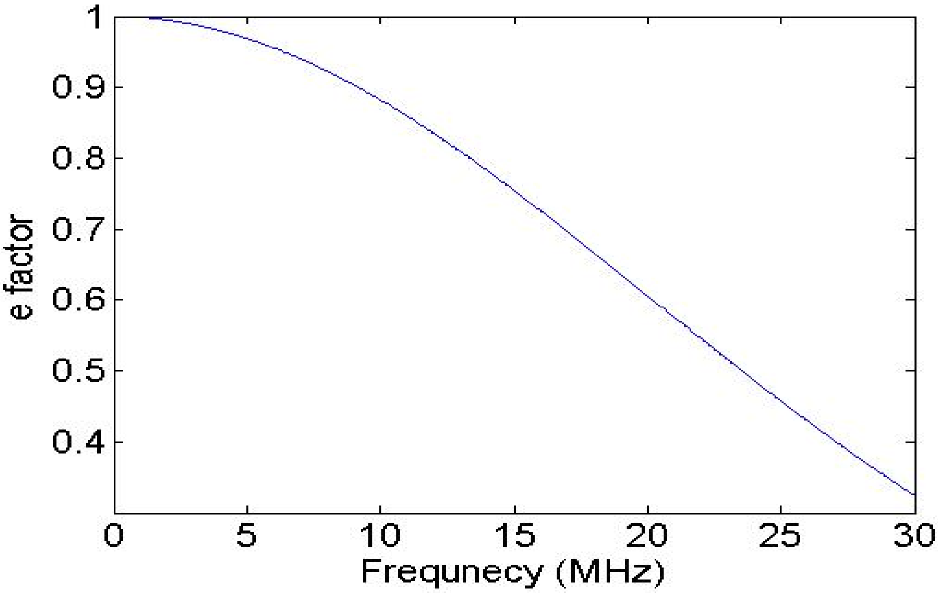

(a)

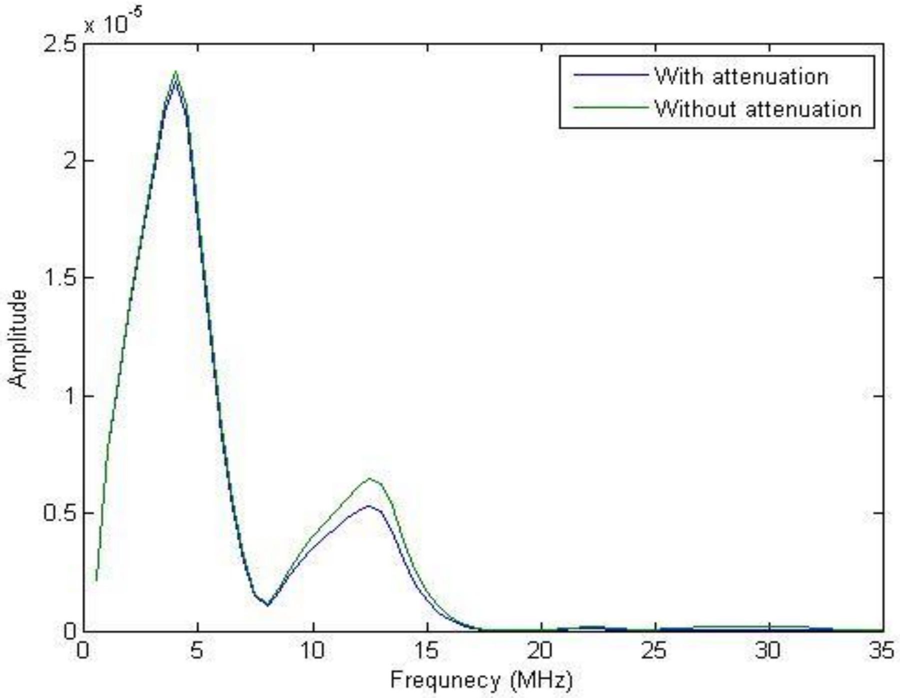

(b)

Figure 21. On a) a plot can be seen of the transmission through a 50 mm water layer due to frequency dependent attenuation. b) shows the how big the influence of attenuation is on a simulated signal from a microsphere placed at 50mm from the detector.

4.1.2 Resolution

To determine the resolution, measurements of small objects with known, sub-resolution size were conducted, where the full width at half maximum (FWHM) of the profile in every direction was taken as an estimation of the size of the point spread function (PSF).

The following phantom was prepared: we took three polystyrene black dyed $\sim 100\mu m$ microspheres and put them in a 2% agar solution.

The sample was then mounted on the rotary stage and was embedded in a water bath. The laser used here was the Innolas Spitlight 600 OPO, which was tuned to a wavelength of $750nm$.The power of the laser was set to 60% and an energy density filter was positioned after the exit slit. For the output energy we measured a value of $70mJ$. Energy measured at the end of the optical fibres was $E_{left} = 8{,}5mJ \ and \ E_{right} = 8mJ$. The radiant exposure, defined as radiant energy received by a surface per unit area, can be calculated from the known spot size of $8mm$ in diameter, giving about $16\frac{mJ}{cm^2}$ from each side. The acquired data was used to generate the reconstruction shown in Fig. 22., which displays the maximum amplitude projections (MAP) in all directions.

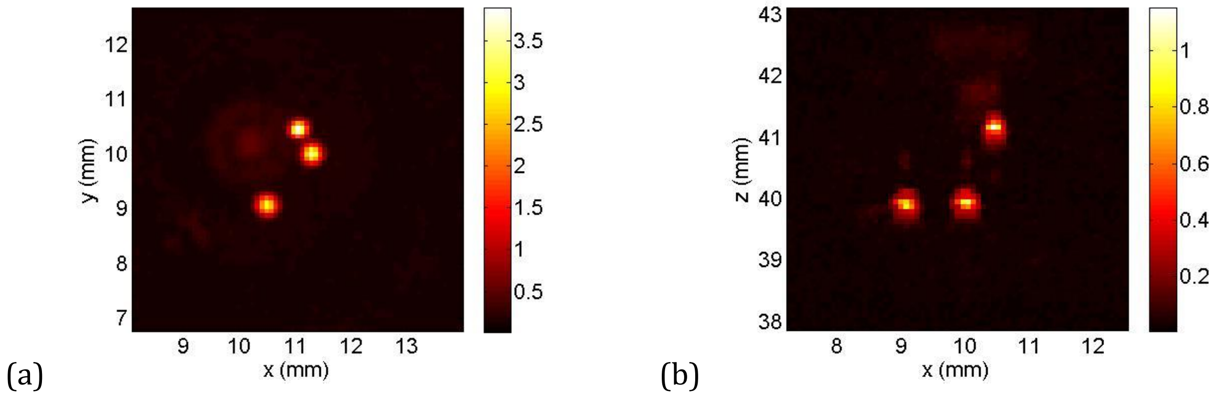

(a)

(b)

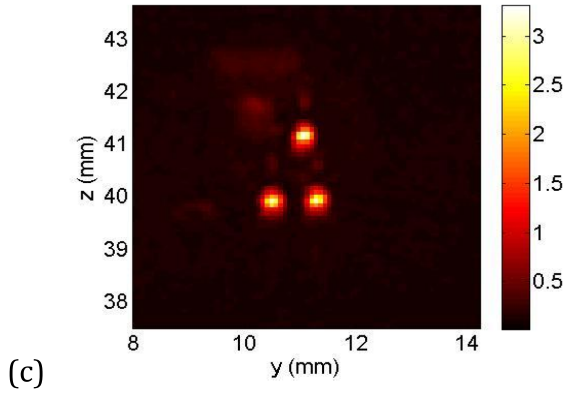

(c)

Figure 22. MAP of microspheres embedded in agar, seen from three different orientations.

To estimate the size of the PSF, a slice through each sphere in all possible directions was extracted and profiles through the centre were calculated. Then we took the FWHM as the value of the apparent size of the sphere in each spatial direction. In Fig. 23 this is shown only for one of the spheres, but it is worth mentioning that all of them had the same size.

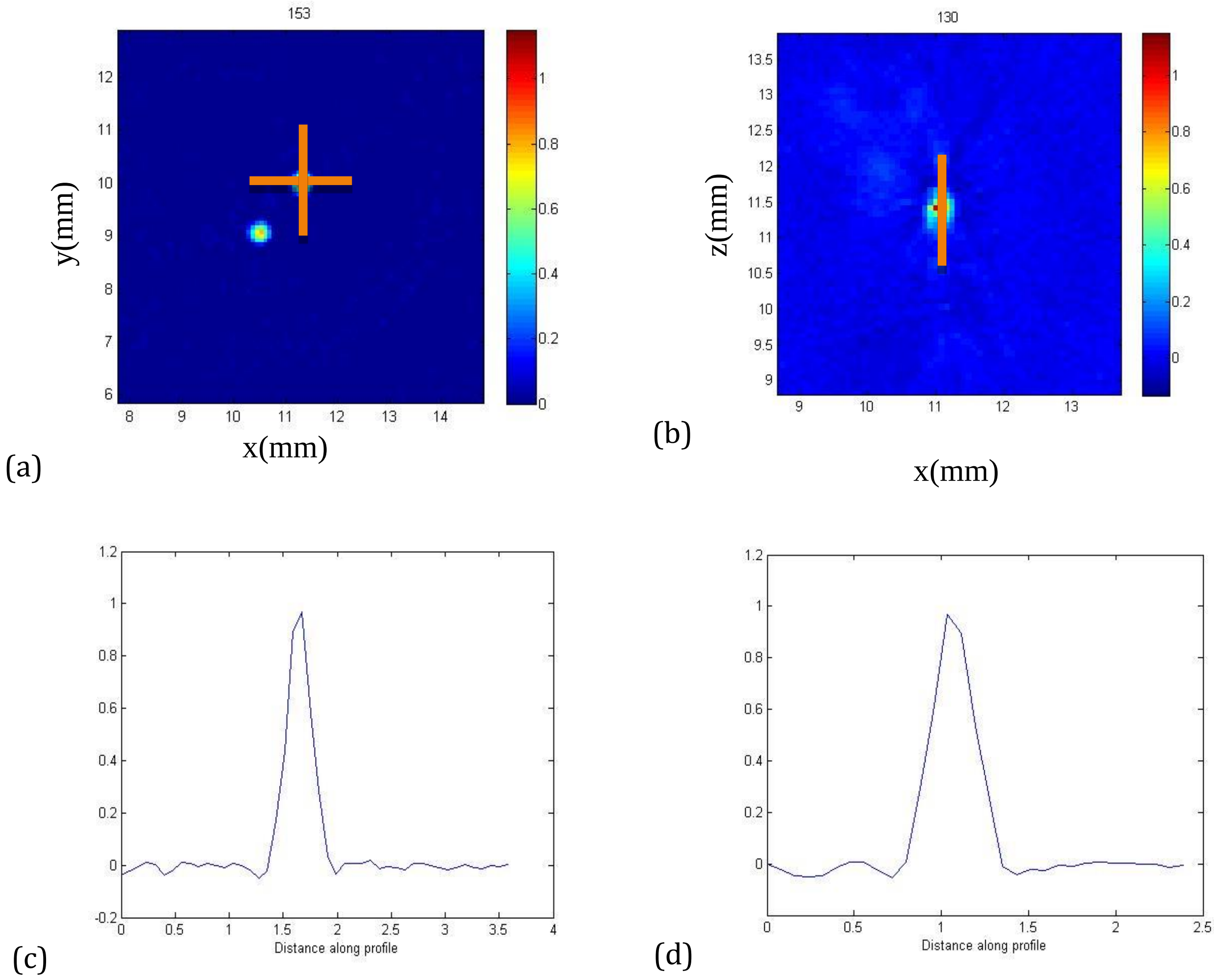

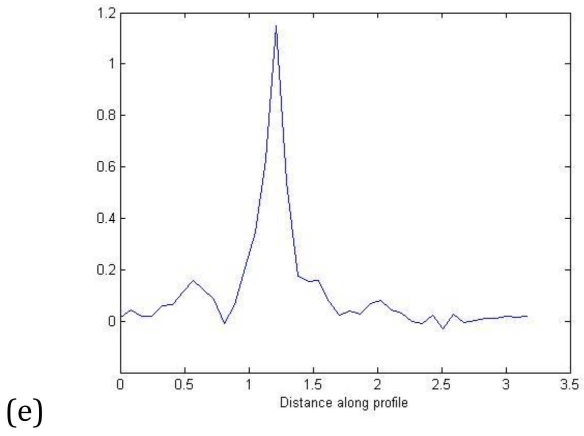

Figure 23. a) Placement of profiles on each sphere in x and y direction in order to determine their size. b) Profile in z-direction. c), d) and e) show the extracted profiles, from which we estimate the size of the PSF, by taking the FWHM value.

From the profiles it can be estimated that the apparent size of the sphere in each direction is about $\sim 200 \mu m$. This is a good estimate for the size of the PSF, since the real diameter of the spheres is significantly smaller. Objects with a size smaller than 200 µm will appear blurred in the reconstructed image and will not be quantitatively evaluated. This leads to the conclusion that the resolution of the tomograph is approximately equal or better than 200µm.

4.1.3 Sensitivity

The main goal of this experiment was to determine the limit in terms of optical absorption coefficient, at which a photoacoustic source cannot be distinguished from the noise.

Here we took two small flexible tubes with a diameter of $1mm$ and filled them with an absorbing liquid (Orange-G solution in water, $1g/L$). The two tubes were then crossed and put in a 2% agar solution mixed with milk-like fluid for better illumination. The transmission spectrum of the Orange G solution and its absorbance are shown in Fig. 24

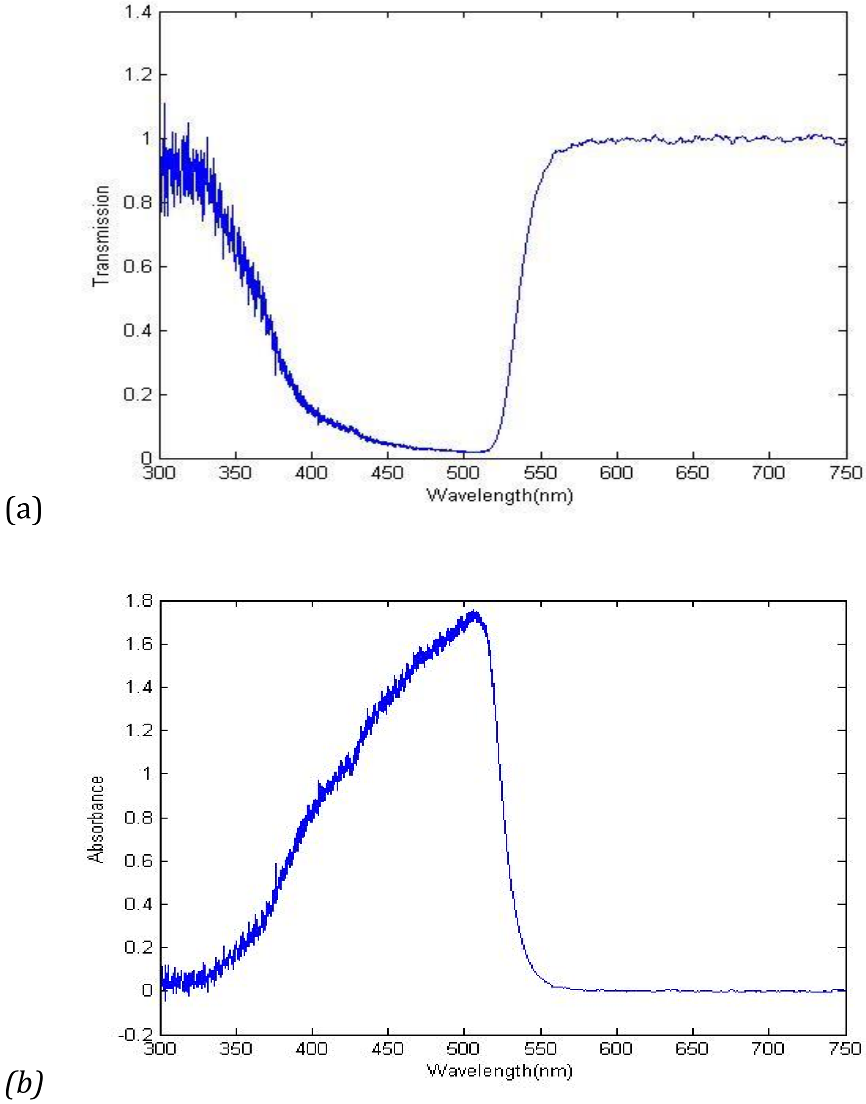

Figure 24. a) shows the transmission spectrum of Orange-G with reference to water. On b) the absorbance spectrum is plotted

Water was used as reference for the calculation of the absorption coefficient. The relationship between absorption coefficient and wavelength is shown in Fig. 25.

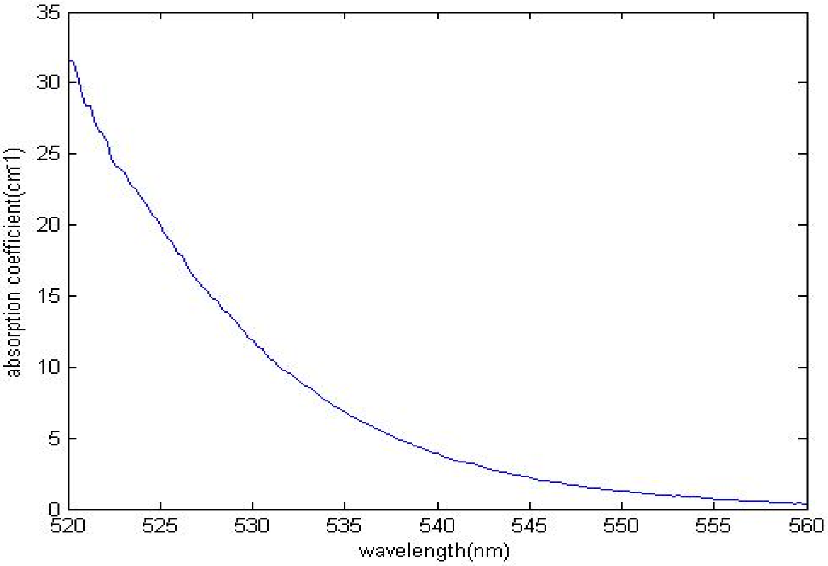

Figure 25. Relationship between absorption coefficient and wavelength of Orange-G

The dye solution shows a strong drop in absorbance in the green spectral range between 520nm and 560nm. Measurements of the phantom were taken at 520nm, 528nm, 535nm, 540nm, 545 nm and 550nm, where the sample was illuminated by laser light from both sides, with pulse energies of $4{,}2mJ$ and $4{,}5mJ$ respectively. A reconstructed image can be seen on Fig. 26**.**

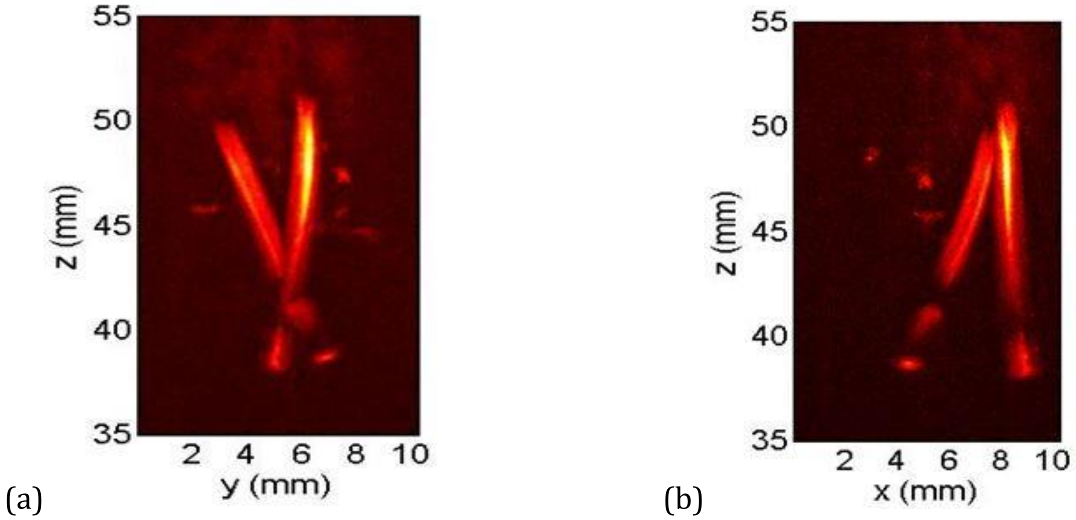

Figure 26. Maximum amplitude projections of the phantom image seen from two different directions.

For all wavelengths the same x-y-slice of the sample was chosen. A small rectangular area inside the sample was then selected and the mean value and the standard deviation of all the pixel intensities inside the rectangle were taken for each wavelength.

In Fig. 27. the slices that were used for the evaluation can be seen.

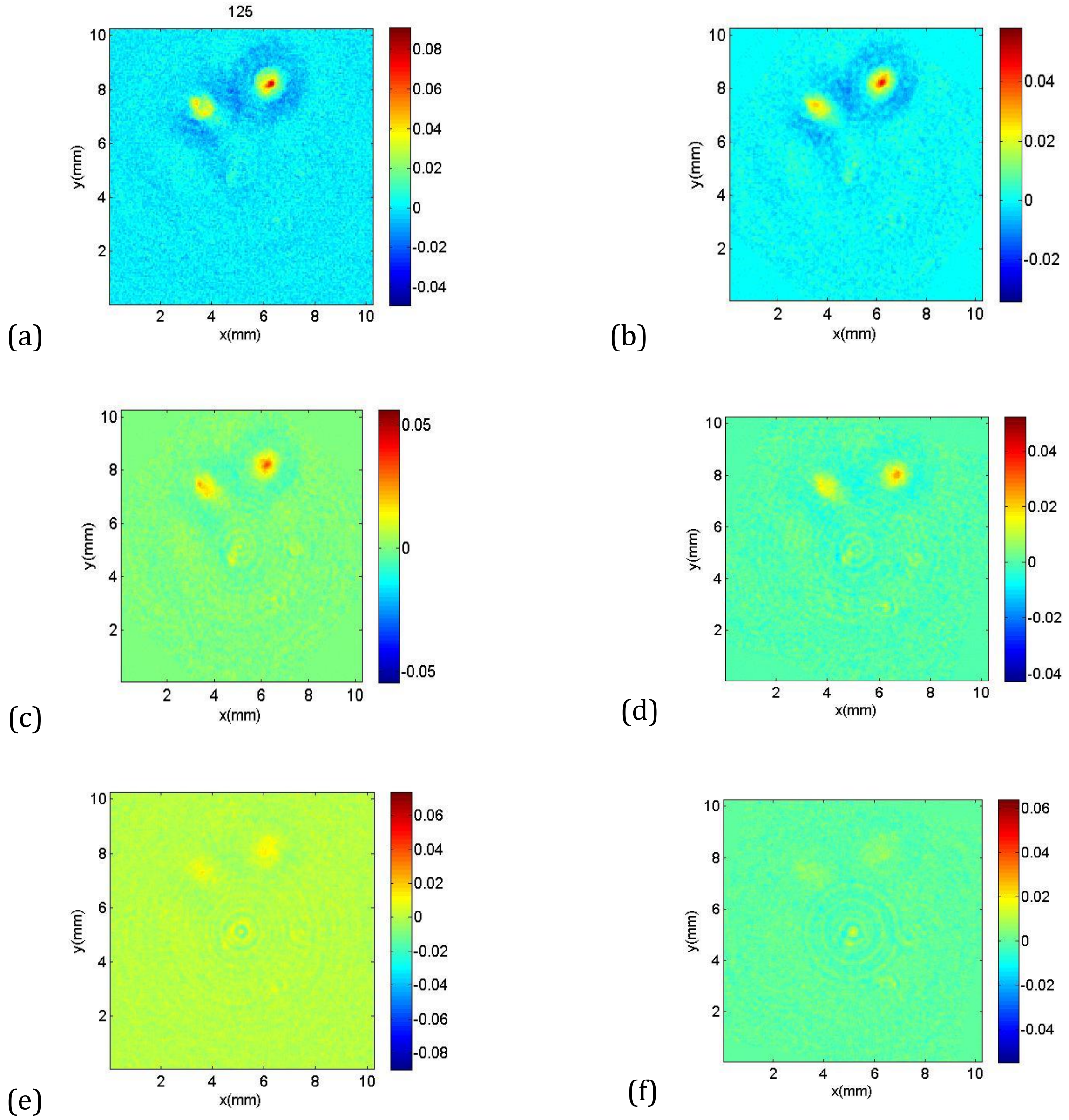

Figure 27. Slices through the sample at wavelengths a) 520nm, b) 528nm, c) 535nm, d) 540nm, e) 545nm, f) 550nm

Fig. 28 represents the result, showing the relationship between amplitude of the signal and the absorption coefficient at different wavelengths, where the red points represent the mean amplitude value inside the chosen rectangle for the different wavelengths.

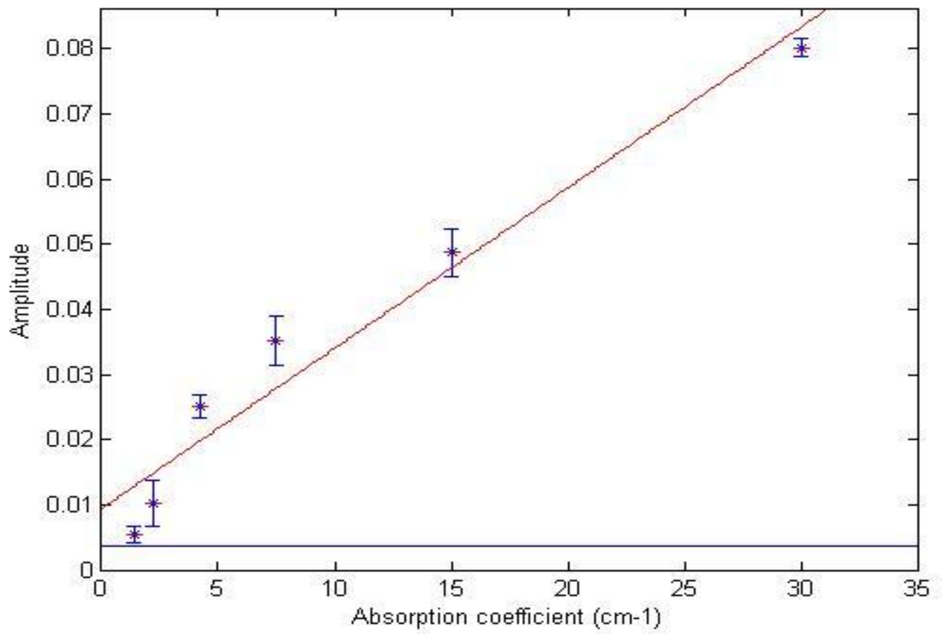

Figure 28. Relationship between amplitude of the measured signal and absorption coefficient. The blue line in the bottom of the graph represents the noise level. The red points are a measure of the amplitude of the signal at different wavelengths, displayed with their standard deviations. The red line represents a linear fit.

The noise level was determined by also selecting a rectangular area in the image, where no signal was measured, and the root mean square (RMS) value of all of all the points in this area was taken. The result was $RMS_{noise} = 0.0034$, which is illustrated as a blue line on Fig. 28. From the result displayed in Fig.28 it can be concluded that objects with an absorption coefficient $< 5cm^{-1}$ cannot be clearly distinguished in a PA image from noise. A calculation of the signal-to-noise ratio for every wavelength and corresponding absorption coefficient confirms this result as seen in the next table.

Table 3. Signal to noise ratio for different absorption coefficients

Wavelength$[nm]$	**Absorption Coefficient**$[cm^{-1}]$	**SNR**
520	30	24
528	15	14
535	7.5	10
540	4.2	7
545	2.2	3
550	1.4	1.5

4.2 Optimization

For the better functionality of the device the following corrections had to be made.

4.2.1 Corrections

A correction had to be made for the distance between every line detector and the centre of the arc. The reason for this correction originates from gluing the circuit board to the base. The glue layer in between is not uniformly thick, which leads to variation in the distances. By specification the radius of the circular array is supposed to be exactly $r = 50mm$. To determine if this is true, a small sphere with a radius of about $\sim 1mm$ was placed in a 2% agar solution and was positioned near the center point of the line sensor array. The following procedure was followed: firstly, the time for the acoustic signal to reach each sensor was measured. Under the assumption of a constant radius of the arc of 50 mm a fit curve was then calculated for the arrival time of the signals to each sensor. Taking the difference between the fitted and measured times the exact position of each transducer was obtained. The radius of the sphere was taken into account in this calculation. The correct distance of each sensor from the centre of the array is seen on Fig. 29. The corrected values were used in the reconstruction algorithm in order to obtain the exact position of the sample with respect to each sensor.

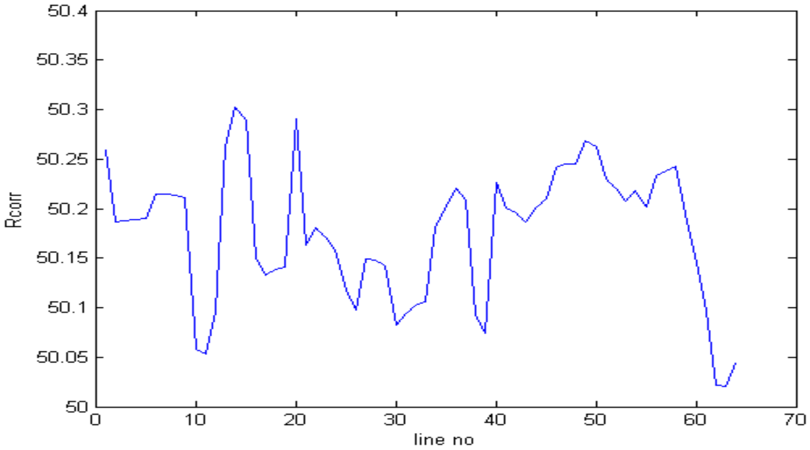

Figure 29. Corrected values of the radial distance of each sensor

Another correction for the sensitivity of different sensors had to be made, because it turned out that signals from the same source were received with quite different amplitude. The reason was most likely again the varying thickness of the glue layer between PVDF film and copper electrodes. The correction was made by measuring the signals, originating from an $\sim 3mm$ oil sphere positioned in agar, near the centre of the arc. Since the sphere is expected to generate a uniform wave in all directions, the reciprocal signal amplitudes registered from each sensor could be used as the calibration factors shown in Fig.30. To use these values for image formation, measured signals are multiplied with these calibration factors prior to reconstruction.

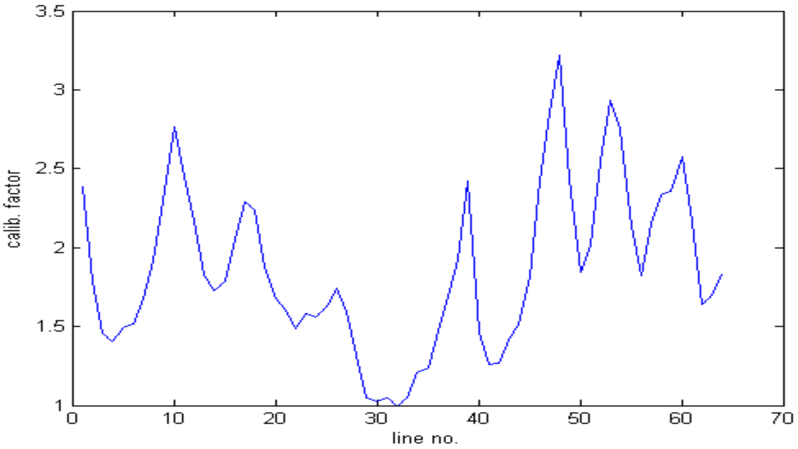

Figure 30. Correction factor for the amplitude of the signal of every sensor

These two corrections were saved and applied to future measurements. Here it is also important to show how these corrections influence the reconstructed image. On Fig. 31 four projections of a hair can be seen, which is tied in a loose knot in the middle. A comparison with and without corrections is made. These images show that the made corrections have a big influence on the final results. The correction for the sensitivities of the different sensors corresponds only to an increase in the amplitude values of the measured signals (compare Fig. 31 c and d). The correction for the distances to each sensor however (compare Fig. 31 b and d) accounts for a better reconstruction, by making sure that signals are back projected to the correct location in the reconstruction plane.

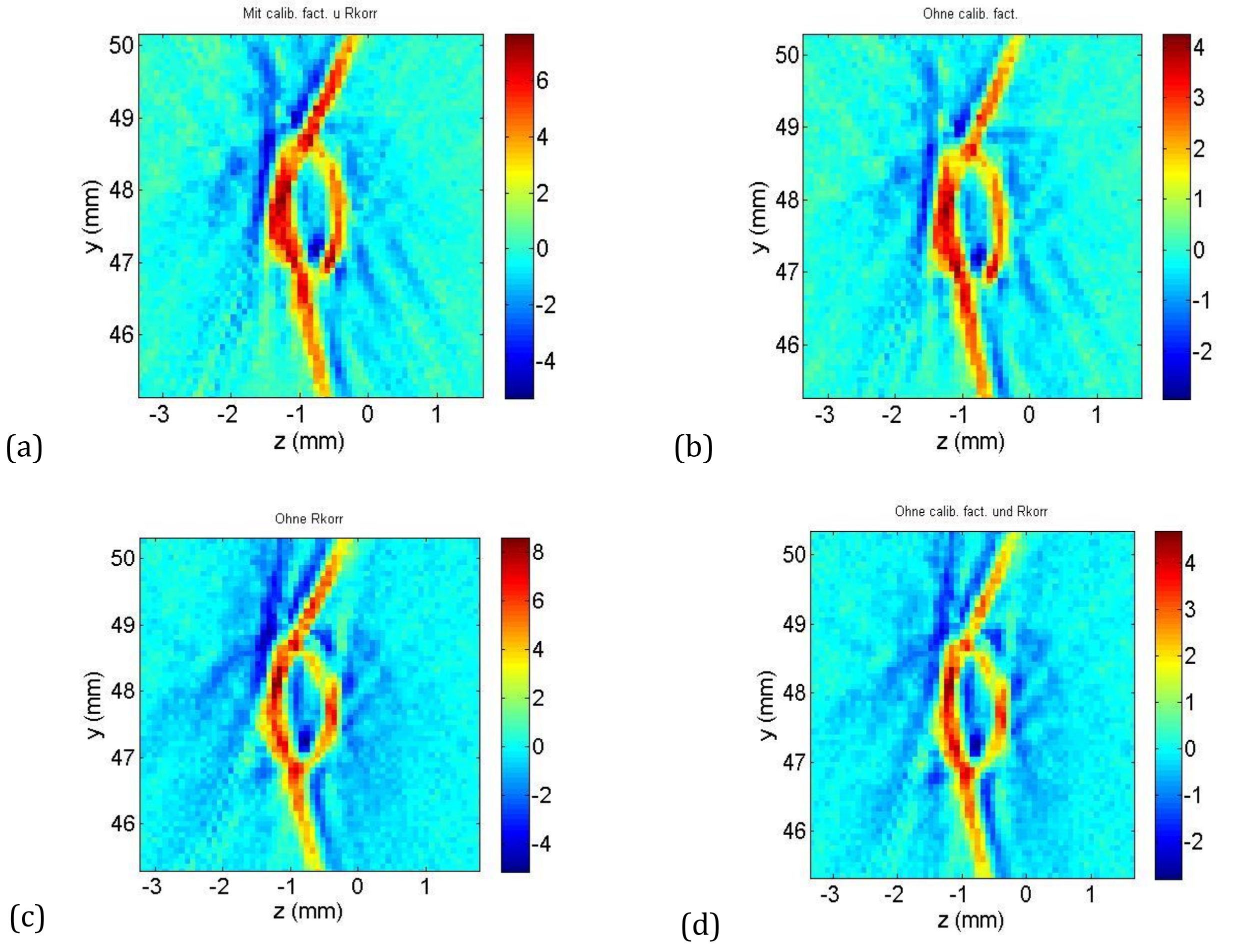

Figure 31. Influence of the made corrections for the positions and sensitivities of the individual sensors. a) With corrected positions and amplitudes, b) with corrected positions only, c) with corrected amplitudes only, d) without any corrections.

As mentioned before the speed of sound depends strongly on temperature. For the optimization of the accuracy of future measurements and for the improvement of the quality of the reconstructed images, a program has been incorporated in the reconstruction algorithm that takes into account the temperature of water and calculates the speed of sound for that temperature. To show why this is so important, a temperature $2^{\circ}C$ higher than the measured temperature was used for the reconstruction to see what impact this has on a projection image. Fig. 32 shows a projection image of a hair, tied in a knot, embedded in agar solution.

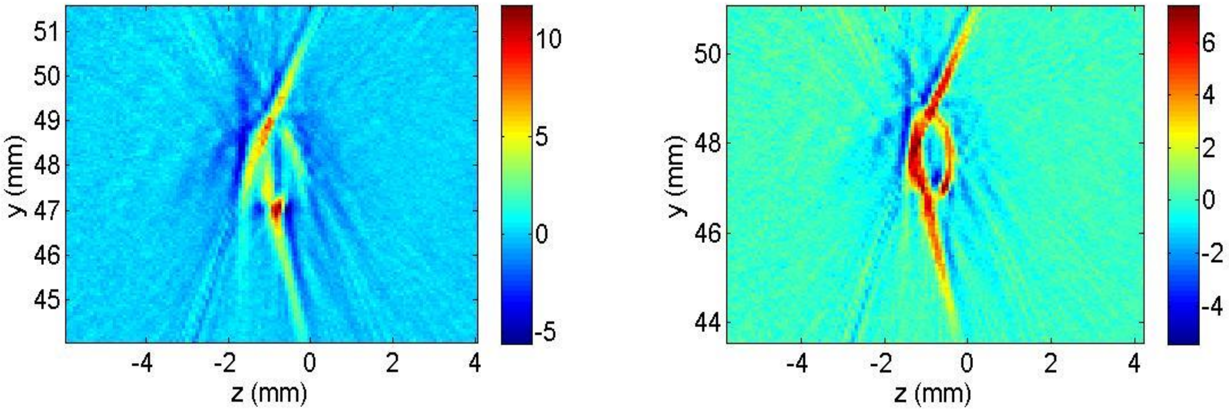

(a) (b)

Figure 32. Influence of temperature on the reconstruction. a) shows the influence on the reconstruction of a $2^{\circ}C$ *temperature change, b) shows a projection of the imaging object at the temperature measured during the experiment.*

4.2.2 Sample preparation

An optimization has been made to the way how the sample is prepared and mounted. For better illumination of the sample a milk-like fluid is mixed with agar. The sample is placed in agar in a small polyethylene cuvette, which can then be easily mounted on the rotary stage. Although the difference in acoustic impedance between polyethylene and water is minimal, the difference in speed of sound is significant. Therefore, after conducting a series of experiments it has been established that the cuvette has a strong influence on the reconstructed pictures. This is why the cuvette is cut on the bottom side so that the sample can be pushed out of it, thereby avoiding the plastic layer between sample and surrounding water.

4.3 Measurements

4.3.1 Chicken heart

When illuminating biological samples with green light, it is strongly absorbed and has a much lower penetration depth compared to light in the red part of the spectrum. Here we try to confirm this by taking measurements of a chicken heart. A small slice, taken from the middle part of the heart, was embedded in a 2% agar solution and then mounted on the rotary stage. By illuminating it from both sides with short laser pulses the pressure signals were recorded for each angle at two different wavelengths – $540nm$ and $630nm$. To reduce noise, the measurements were smoothed over four laser pulses. Here the Continuum Nd: Yag laser was used as a pulsed light source, where we registered an energy of $E = 5.4mJ$ per fiber at 540 nm and $E = 2mJ$ at 630 nm. Output energy of the laser was also determined to be about $20mJ$ at $540nm$ and two times less at $630nm$. Temperature of water was also monitored. During this experiment we measured a value of $T_{(540)} = 26.1°C$ and $T_{(630)} = 25.7°C$.

For evaluation of the results a slice from the reconstructed image was chosen in the x-y-plane. A profile was then extracted in the x-direction. Through the profiles we determine the penetration depth of the incident light, by taking the FWHM of the peak near the surface.

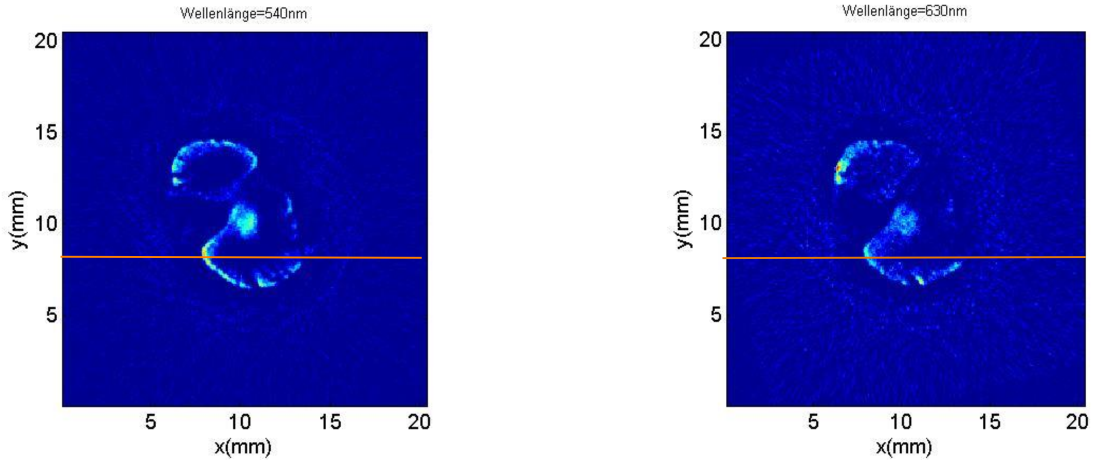

(a)

(b)

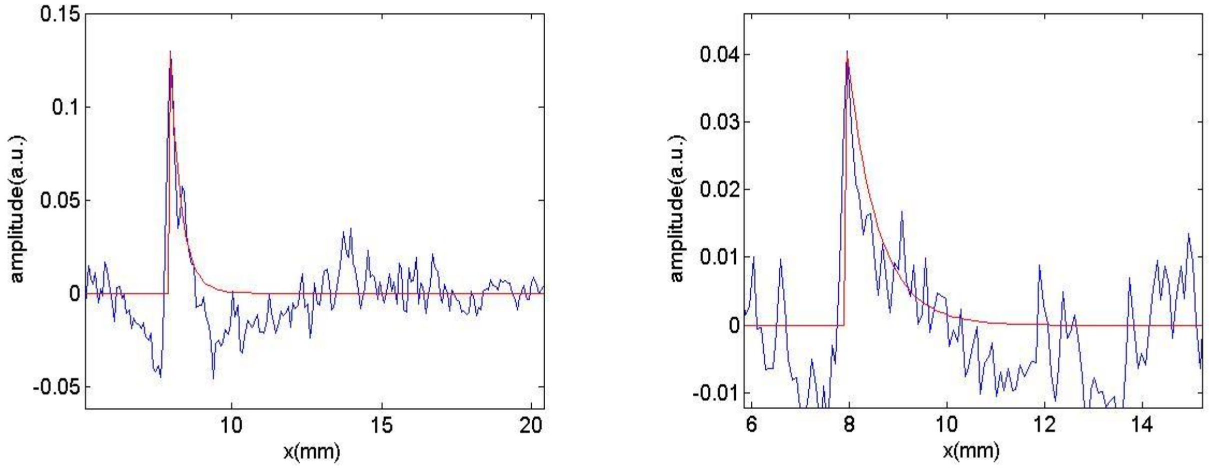

(c) (d)

Figure 33. a) and b) show slices through the chicken heart sample at 540 nm (a) and 630 nm (b). c) and d) are the profiles along the lines as shown in a) and b), showing the penetration depth of the incident light at two different wavelengths (540nm and 630nm). The red line that can be seen on c) and d) is the fitted curve for each measurement.

An exponential curve was fitted for better evaluation of the penetration depth. We register a penetration depth of about $0.370mm$ for green light and of about $0.650mm$ for red light, which proves the statement made earlier.

4.3.2 Blueberry

A small blueberry was prepared by peeling its skin and placing it in a 2% agar solution. Temperature of water is measured to be $T_w = 28^{\circ}C$ during the measurement. Light, illuminating the sample, was in the green spectral range at 540nm, where we measured $E_1 = 5.2mJ$ and $E_2 = 5.4mJ$ output energy at the end of each fibre. The first two images on Fig. 34 are an evidence for how the sample looks like in reality and the second two illustrate the specimen cut in halves.

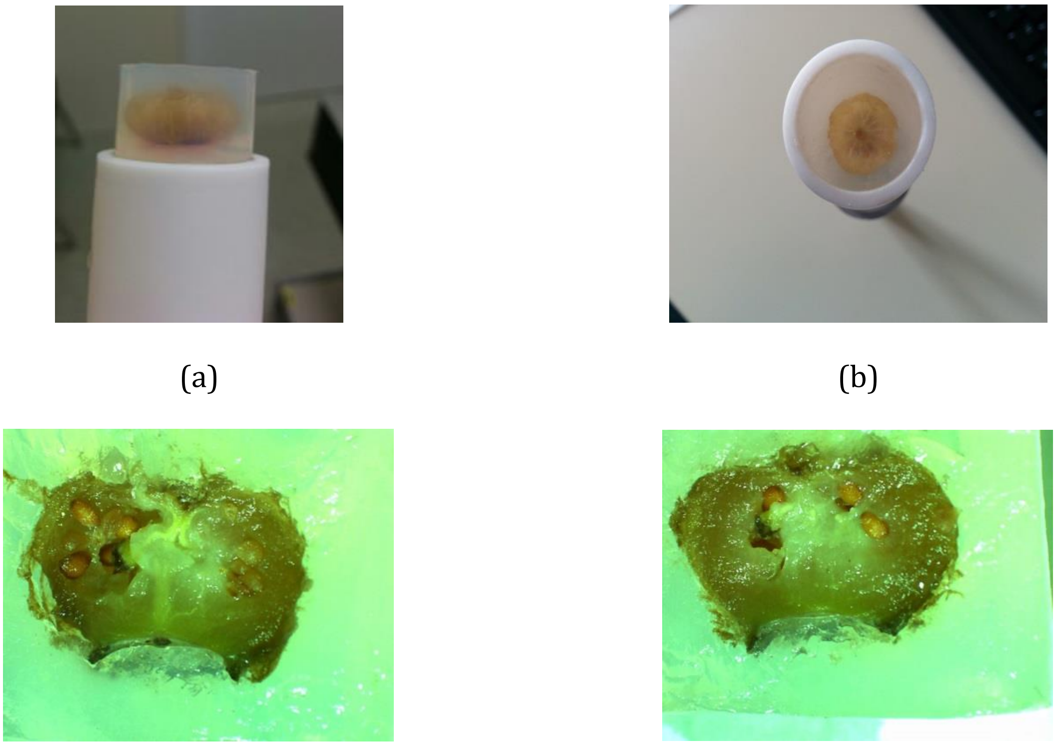

(a) (b)

(c) (d)

Figure 34. Blueberry in agar. The skin of the blueberry has been peeled off. a) and b) show a view of the blueberry from the side and from the top. c) and d) are pictures of the sample, which was cut in halves, taken with an optical microscope.

On Fig. 35 we see three MAP projections, where the blueberry can be seen from three different directions. In these reconstructed images we can clearly distinguish between the individual fibres, which absorb light strongly at $540nm$.

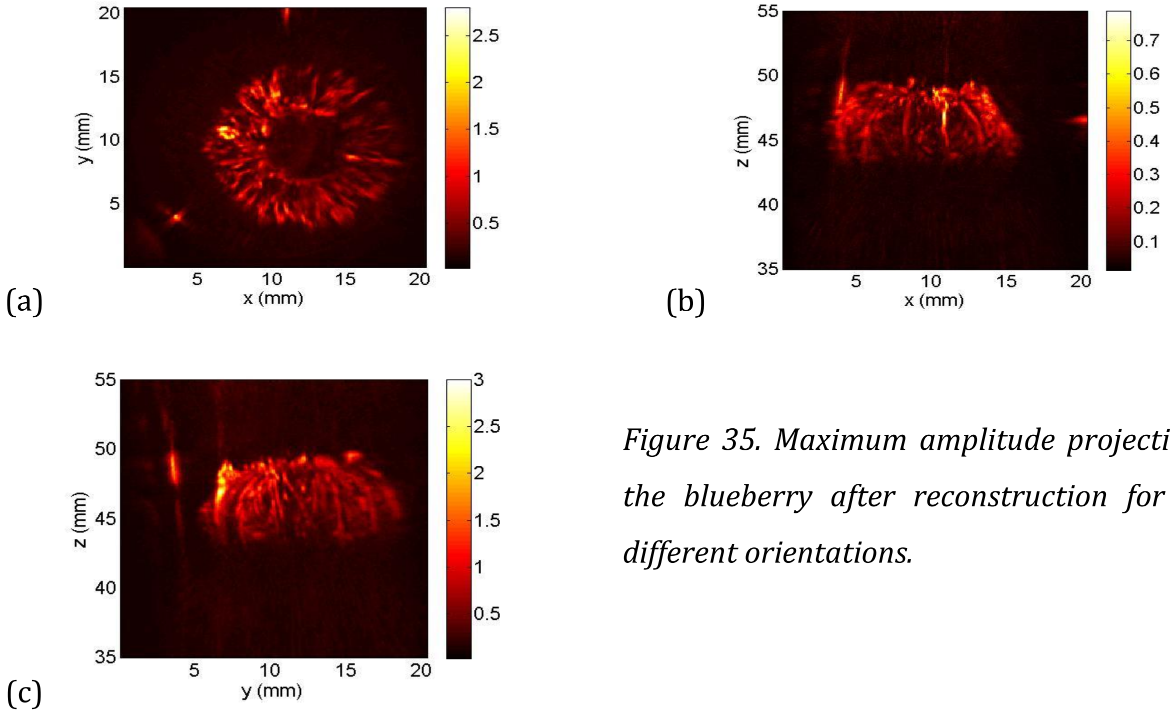

(a) (b) (c)

Figure 35. Maximum amplitude projections of the blueberry after reconstruction for three different orientations.

Here one of the goals was to see if the seeds inside have absorbed any light and if we can figure out how deep they were positioned under the surface of the blueberry. After reconstructing the initial pressure distribution, we took a vertical slice of the sample. The fibers of the blueberry have absorbed a portion of the incident light, but part of it penetrated into the sample and was absorbed by the seeds. This can be seen in Fig. 36. We took a profile, as shown in Fig. 36 a) to determine the distance between an outer layer point of the blueberry and the particular seed that we see on the slice image. This distance is estimated to be $\sim 3mm$.

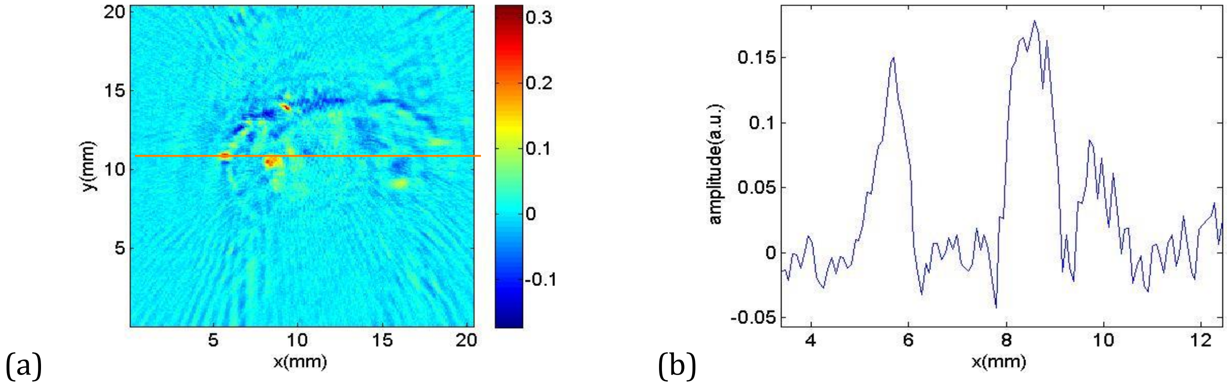

(a) (b)

Figure 36. a) Slice through the blueberry in y-direction. b) Profile, as seen on a), showing the depth, at which the seed is found.

4.3.3 Crossed painting brush bristles

To further optimize the tomograph and to increase the quality of our reconstructed images, the number of averages was increased to 8, leading to a total of 6400 laser pulses for the acquisition of the imaging data. The results were then compared with the results obtained from four times averaged data with a total of 3200 pulses. The sample was rotated for both cases first over 180° and then over 360°. When illuminating a sample from both sides, for 180°C rotation we have sufficient data for accurate image reconstruction. We then compare SNR values for both of these cases as well.


(a) (b)

Figure 37. Optical images of the used sample, seen from two different orientations

The phantom, as seen on Fig. 37, is made out of painting brush bristles that were crossed in different directions in a 2% agar gel solution. Measured output energy of the two fibers was $E_1 = 4.4mJ$ and $E_2 = 5.5mJ$, respectively, for an input wavelength of $540nm$. Water temperature values of $T_{w(6400pulses)} = 27.8°C$ and $T_{w(3200pulses)} = 28.3°C$ were measured and then used for calculation of the speed of sound. The results of this experiment are summarized in the next table.

Table 4. Signal to noise ratio for different rotation angles of the sample and different numbers of averages

	SNR	Noise RMS	Max. Pixel Value
180°, Averaging rate = 4	139	0.0124	1.5196
360°, Averaging rate = 4	158	0.0103	1.2713
180°, Averaging rate = 8	81	0.0210	1.7136
360°, Averaging rate = 8	119	0.0127	1.5057

The result shown here is quite unexpected. Although the advantage of averaging is evident in the experiments when comparing the single shot signals with the four times averaged ones (not shown), an increase from 4 to 8 times averaging does not improve the SNR. This may be due to slight movements of the sample during the measurement. A slight improvement in SNR was observed for 360° rotation compared to 180° but was not very significant. From this experiment it can be concluded that the combination used for most of the experiments in this work (4 times averaging, 360° rotation) was the optimum choice. Investing more time in more averages does not yield the expected improvement.

4.3.4 Mouse kidney

For this measurement a kidney was freshly excised from a white mouse and embedded in a 2% agar solution. The kidney had a size of about 1 cm. It was illuminated from both sides with short laser pulses in the NIR at $750nm$ with energy $E_{left} = 20mJ$ and $E_{right} = 10mJ$. With a diameter of the laser beam of 1.5cm the radiant exposure values were about 11,31 mJ/cm² and 5,65 mJ/cm². To reduce noise, the detected signal was averaged 4 times. The sample was first imaged with a camera (Fig. 38).

(a) (b)

Figure 38. Optical images of a mouse kidney from two sides.

It was expected that a contrast will be generated by the blood vessels underneath the surface. On Fig. 39 the MAPs are displayed.

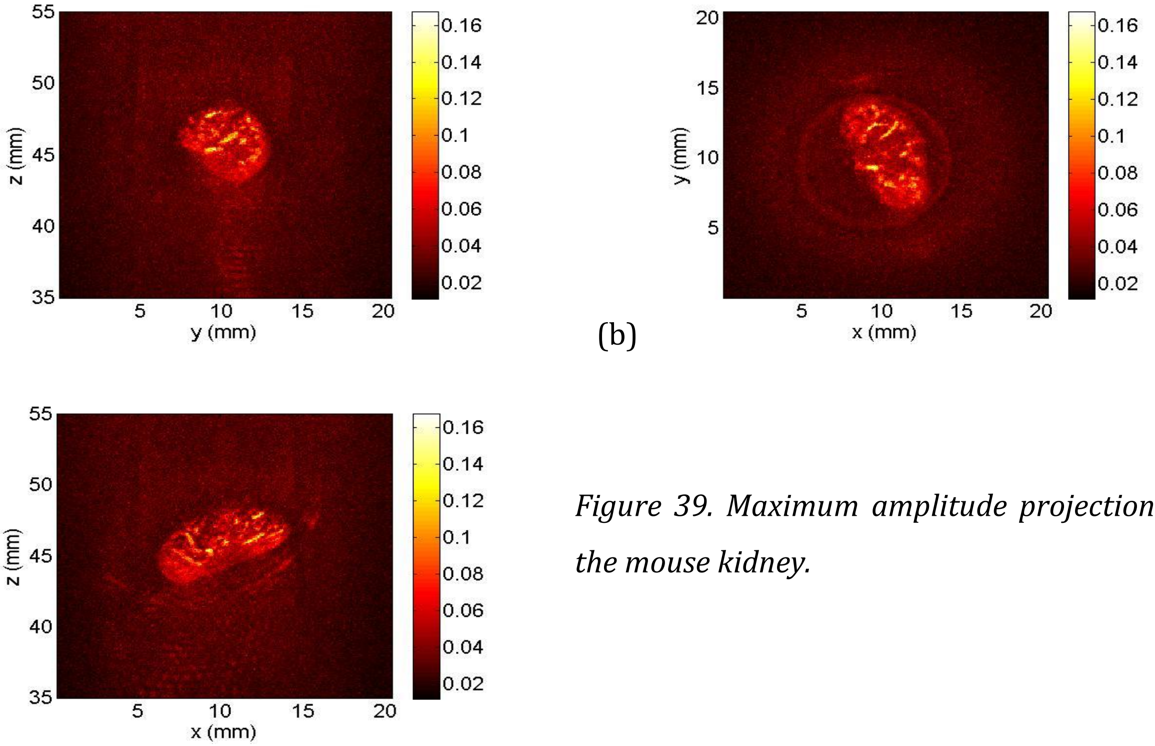

(a) (b) (c)

Figure 39. Maximum amplitude projections of the mouse kidney.

The bright lines that can be seen on all three pictures are coming from the blood inside the vessels lying underneath the surface, as expected. To better demonstrate this a slice through the sample is displayed on the next Fig. 40. Blood absorbs light more strongly than the surrounding tissue in the near infrared, which is the reason for the contrast visible in the PA images.

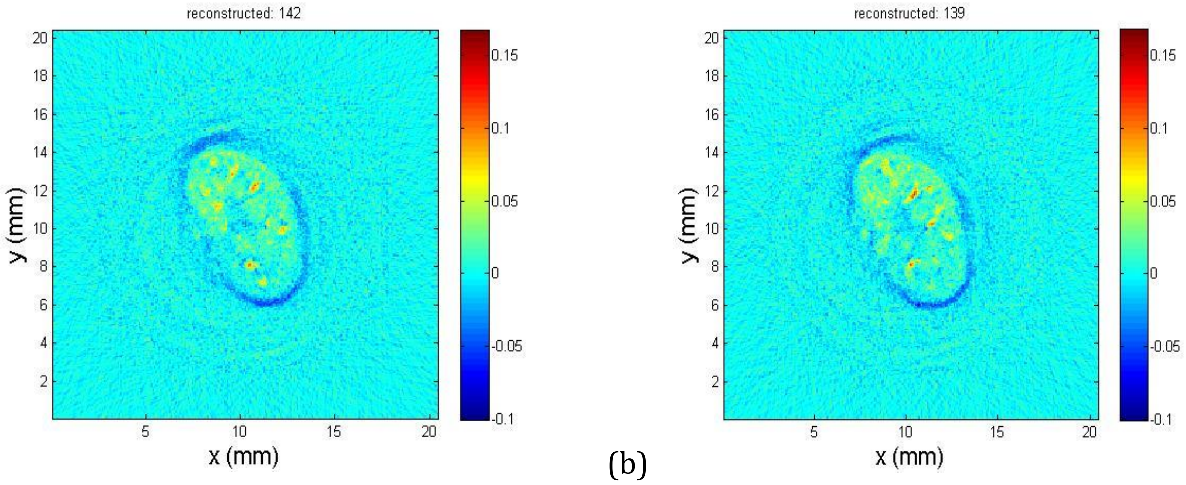

(a) (b)

Figure 40. Two different x-y-slices of the sample, showing the absorbing blood vessels underneath the sample surface.

After the reconstruction we estimated that the sample had a size of about 1cm, which corresponds to the real size of the kidneys. The blood vessels were roughly at 1mm under the tissue surface.

4.3.5 Mouse Brain

The specimen was placed in a 2% agar gel and mounted on the rotary stage. It was first imaged with an optical camera (Fig. 41).

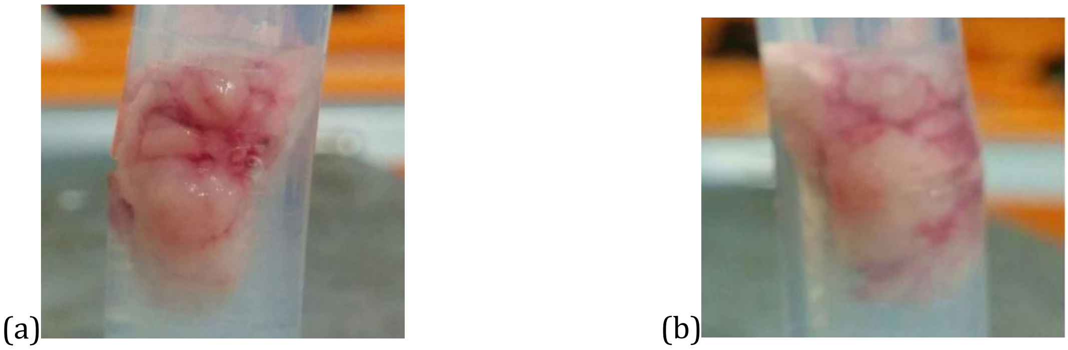

Figure 41. Optical images of a mouse brain, embedded in agar gel

The only absorbers here are the blood vessels, some of which can be seen on the surface of the sample. The surrounding tissue scatters light strongly but does not provide a measurable signal due to its low absorption coefficient. During measurements the laser wavelength was tuned to 750nm and the averaging rate was set to 4.

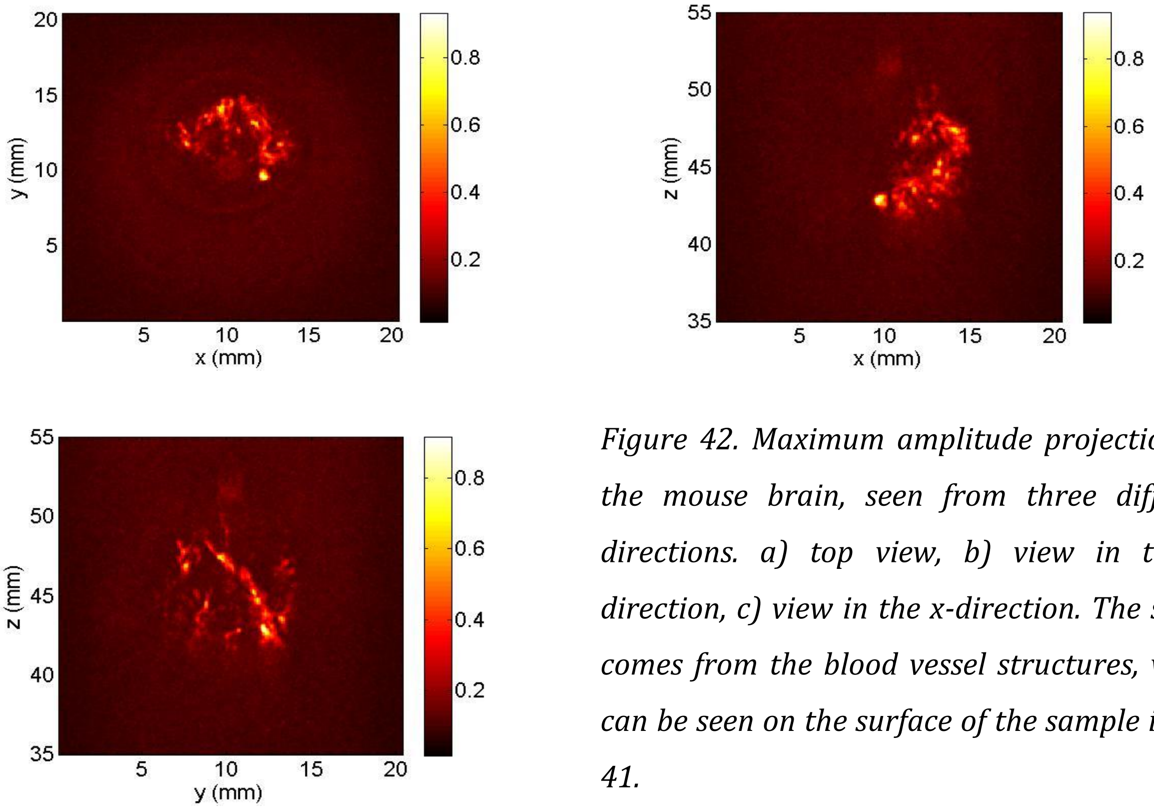

Figure 42. Maximum amplitude projections of the mouse brain, seen from three different directions. a) top view, b) view in the y-direction, c) view in the x-direction. The signal comes from the blood vessel structures, which can be seen on the surface of the sample in Fig. 41.

In Fig. 42 b) we see the MAP from the side, where the structure is comparable to the one on image in Fig. 41 b). The bright structures in all of the projection images are vessels containing blood.

4.3.6 Chicken embryo

The embryo was in a stage where the eyes had grown enough to be distinguished. They appeared black so it was expected that a huge amount of the measured signal will be coming from them. Optical images were taken as well (Fig. 43).

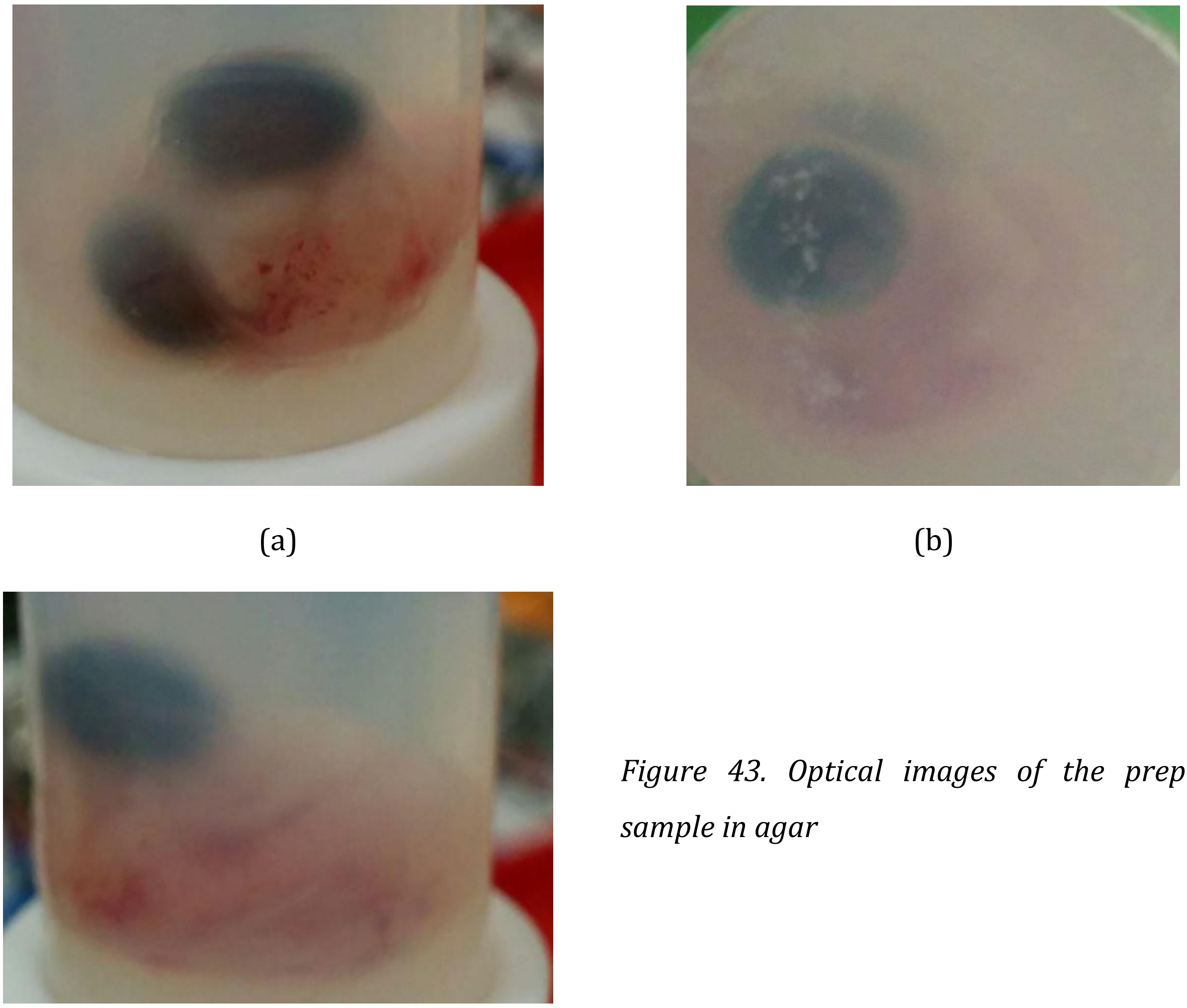

(a)

(b)

(c)

Figure 43. Optical images of the prepared sample in agar

In these images not only the eyes but also blood vessel structures are seen. Taking into consideration that blood absorbs light very strongly in the NIR region we assumed that these structures could be also be visualized. The sample was prepared and placed in agar and was illuminated from both sides with 750nm laser pulses, having energies $E_{left} = 20mJ$ and $E_{right} = 10mJ$. On Fig. 44 we can see maximum amplitude projections of the sample for three different orientations.

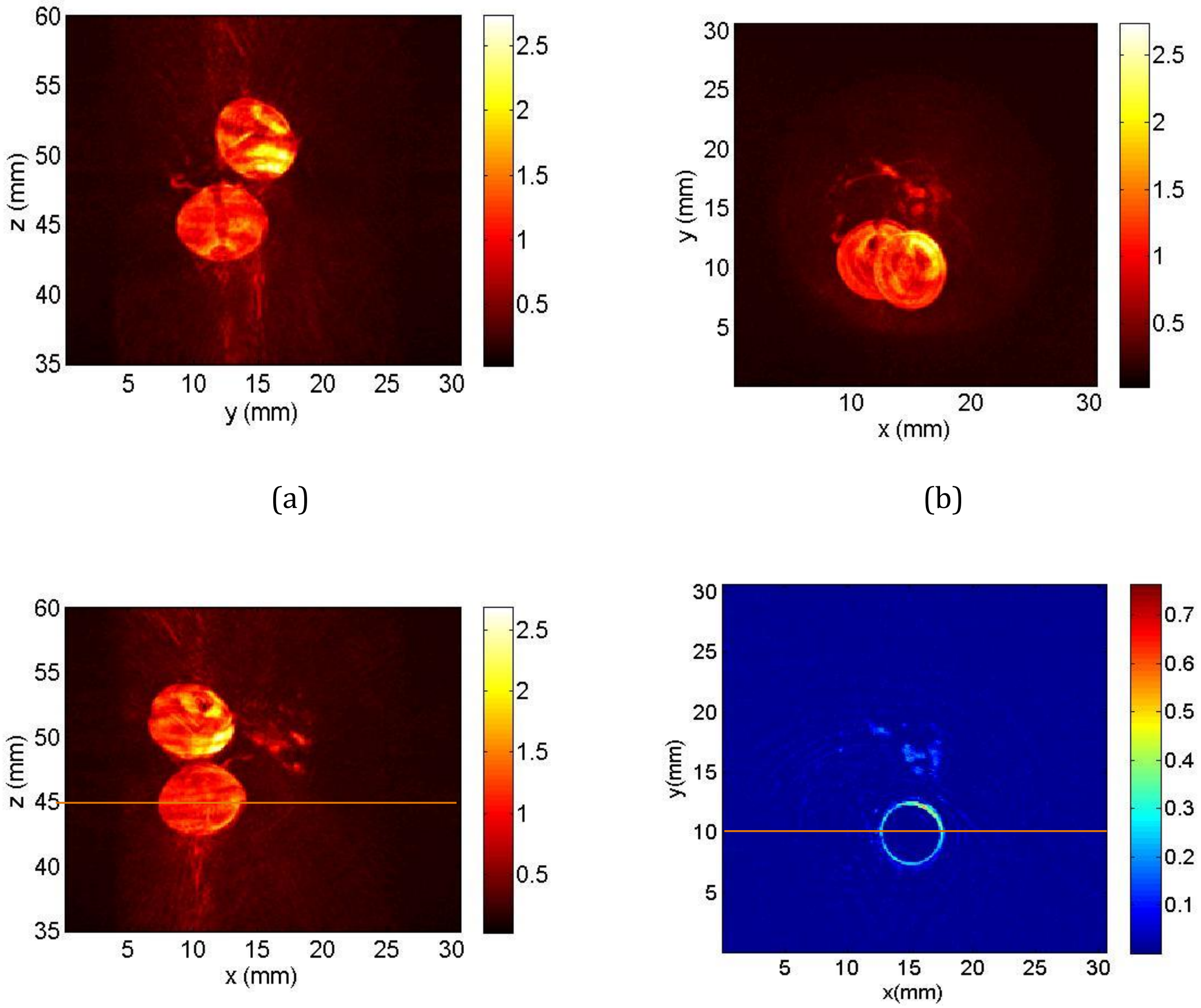

(a) (b)

(c) (d)

Figure 44. Reconstructed images of the chicken embryo. a) view in the x-direction, b) view in the z-direction, c) view in the y-direction. The two spheres here represent the eyes, the structure beside the eyes consists of blood vessels also seen on the optical images. In d) a slice through one of the eyes can be seen, as well as the already mentioned blood vessel structure.

The two spheres here represent the eyes, seen from three different angles. Beside the eyes we see a blood vessel structure, which also appears on the photos on Fig. 42. From the reconstructed images we were able to establish the size of each eye. The upper one was measured to have a diameter of 7 mm and the lower one of about 6 mm. This conclusion was drawn upon taking a slice in the z-direction through the middle of one eye (Fig. 44 d, slice position shown in Fig. 44, c) and looking at the profiles, going through the middle of the sample (red line in Fig. 44, d). The distance between the two peaks, shown on Fig. 45 a) and b) is estimated to be the size of the eyes.

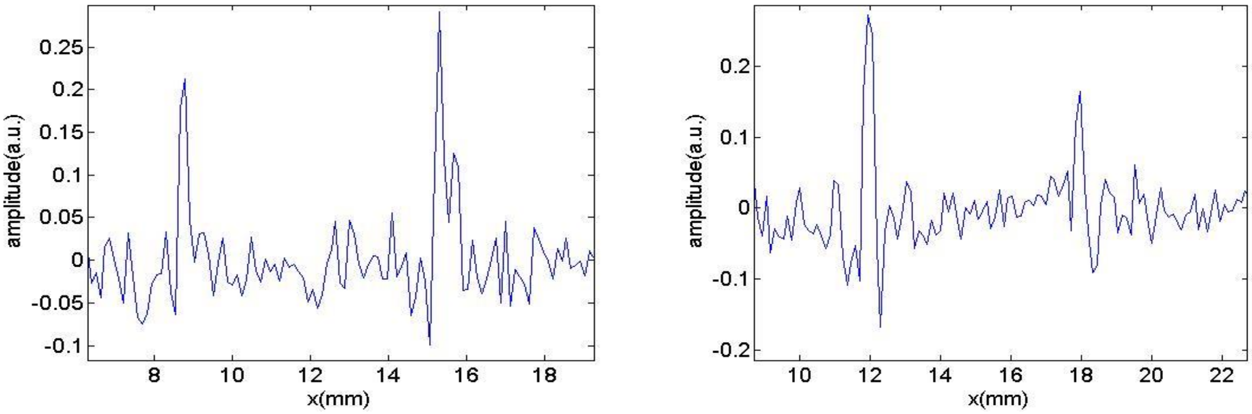

(a) (b)

Figure 45. Profiles, laid through the middle of each eye, in order to determine their size.

5 CONCLUSION AND OUTLOOK

Over the past decade photoacoustic tomography has been rapidly developed in order to improve spatial resolution and sensitivity. It finds more often pre-clinical application, e.g. in small animal imaging, not only as a supporting technique to MRI, but as a standalone imaging modality, due to the non-ionizing character of the irradiation. PAT also finds huge applications in the fundamental sciences, where it is used for characterization of various non-biological and biological materials and samples. The development of the method led to many practical realizations, using piezoelectric detectors or detector arrays and optical detectors.

Here we introduced a device consisting of 64 piezoelectric line sensors, which are positioned on a half cylindrical surface. Compared to other devices based on a single, scanning detector that require long time (on the order of hours) for data acquisition, our array can collect the full range of data, needed for a 3D image, in a matter of minutes. For image formation every point of the sample is being reconstructed from a summation of the signals registered by the sensors for every rotational angle of the specimen. Spatial resolution of the device limits the size of the distinguishable objects to about $\sim 200\mu m$.

Photoacoustic contrast is based on light absorption. To obtain a measure of the sensitivity of the device, we conducted an experiment, showing us what is the minimum absorption coefficient a sample must have in order to provide a strong enough signal. Absorbing structures in an object must have an absorption coefficient of $\mu \geq 5\ cm^{-1}$ for their signal to not vanish in the noise background. It is expected that this value depends on various factors, such as the size of an absorber or the radiant exposure on the surface of the object. Therefore, the value given above can only be regarded as a rough estimate.

PAT still faces some limitations concerning imaging depth, depending on the wavelength-dependent optical properties. For instance, with our device we recorded an imaging depth of about $0.370mm$ for green light and of about $0.650mm$ for red light in chicken heart tissue. Deeper penetration was observed in kidney or brain tissue (1.5mm) of mice, both at 750 nm wavelength. Another biological sample was used to determine the imaging depth in plant tissue. A seed of a blueberry could be visualized at distance $\sim 3mm$ from the surface at 540 nm wavelength.

For better quality of the images the number of pulses and averages can be increased. This leads to longer data acquisition times. On the other hand, a reduction of the required time can be achieved by rotating the sample over 180° instead of 360°, for which still a sufficient SNR was observed.

For future applications the device can be used for tumor characterization. Tumor tissue contains immature collagen and a pronounced network of immature blood vessels. The reason for this is the process of angiogenesis, where new blood vessels are formed from already existing ones. This results in higher blood content in the entire tumor area, which is why the tumor structures appear brighter on images. For signal enhancement optical contrast agents can be used, ideally having high optical absorption in a spectral range where intrinsic chromophores absorb only weakly. They can accumulate in the tumor tissue thus enhancing the optical contrast between normal and tumor cells.

In the case of a heart infarct it can be determined which part of the heart is affected. This region will be badly supplied with blood and will absorb less light. This will result in a smaller measurable signal or no signal at all and the region will appear darker in the reconstructed images[44].

Because the tomograph is built to image small animals having a maximum size of $20mm$, it would be interesting to go in direction of in-vivo experiments and to try to detect blood flow and changes in the hemoglobin oxygen saturation.

6 REFERENCES

[1] A. G. Bell, "On the production and reproduction of sound by light" In: Am. J. Sci. 20, Nr. 118, S. 305–324 (1880)

[2] H. F. Zhang,"Imaging of hemoglobin oxygen saturation variations in single vessels *in vivo* using photoacoustic microscopy". Applied Physics Letters 90 (5): 053901 (2007)

[3] W. Lu, Q. Huang, G. Ku, X. Wen, M. Zhou, D. Guzatov, P. Brecht, R. Su, A. Oraevsky, L. V. Wang, C. Li "Photoacoustic imaging of living mouse brain vasculature using hollow gold nanospheres" Biomaterials 31(9):2617-26 (2010)

[4] R. L. P. van Veen, H. J. C. M. Sterenborg, A. Pifferi, A. Torricelli, E. Chikoidze & R. Cubeddu "Determination of visible near-IR absorption coefficients of mammalian fat using time- and spatially resolved diffuse reflectance and transmission spectroscopy" J. Biomed. Opt. 10, 054004 (2010)

[5] Y. Lao, D. Xing, S. Yang, & L. Xiang "Noninvasive photoacoustic imaging of the developing vasculature during early tumor growth" Phys. Med. Biol. 53, 4203– 4212 (2008)

[6] M. Rui, S. Naramshinhan, W. Bost, F. Stracke, E. Weiss, R. Lemor, M, Kolios, "Gigaherz optoacoustic imaging for cellular imaging" Photons Plus Ultrasound: Imaging and Sensing, ed. Alexander A. Oraevsky, Lihong V. Wang, Proc. of SPIE Vol. 7564, 756411 (2010)

[7] M. Pramanik, G. Ku, C. Li & L. V. Wang "Design and evaluation of a novel breast cancer detection system combining both thermoacoustic (TA) and photoacoustic (PA) tomography" Med. Phys. 35, 2218–2223 (2008)

[8] S. A. Ermilov, T Khamapirad, A. Conjusteau, M. H. Leonard, R. Lacewell, K. Mehta, T. Miller & A. A. Oraevsky "Laser optoacoustic imaging system for detection of breast cancer" J. Biomed. Opt.14, 024007 (2009)

[9] V. E. Gusev and A. A. Karabutov, "Laser Optoacoustics" NewYork: American Institute of Physics (1993)

[10] P. M. Morse and H. Feshbach "Methods of Theoretical Physics" New York: McGraw-Hill, (1953)

[11] J. D. Jackson "Classical Electrodynamics", 2nd ed. Wiley, New York, 1999.

[12] G. B. Arfken and H. J. Weber "Mathematical Methods for Physicists", 4th ed. _Academic, San Diego, CA (1995)

[13] P. M. Morse and H. Feshbach "Methods of Theoretical Physics" McGraw- Hill, New York, (1953)

[14] J. J. Yao, and L. H. V. Wang, Photoacoustic microscopy," Laser & Photonics Reviews, Vol. 7, 758-778 (2013)

[15] M. Grafl Diploma Thesis "Photoacoustic microscopy", Universität Graz (2016)

[16] H. F. Zhang "Functional photoacoustic microscopy for high-resolution and noninvasive *in vivo* imaging". NatureBiotechnology 24 (7): 848-851 (2006)

[17] H. F. Zhang, K. Maslov, G. Stoica and L. V. Wang "Imaging acute thermal burns by photoacoustic microscopy", J. Biomed. Opt. 11(5), 054033 (2006)

[18] M Xu,. H. and L. V. Wang, "Analytic explanation of spatial resolution related to bandwidth and detector aperture size in thermoacoustic or photoacoustic reconstruction" Physical Review E, Vol. 67, 15, (2003)

[19] A. Buehler, E. Herzog, D Razansky. & V. Ntziachristos "Video rate optoacoustic tomography of mouse kidney perfusion". Opt. Lett. 35, 2475–2477. (2010)

[20] A. Taruttis, E. Herzog, D. Razansky & V. Ntziachristos "Real-time imaging of cardiovascular dynamics and circulating gold nanorods with multispectral optoacoustic tomography". Opt. Express 18, 19592–19602. (2010)

[21] X. Wang, D. L. Chamberland & A. D. Jamadar "Noninvasive photoacoustic tomography of human peripheral joints toward diagnosis of inflammatory arthritis". Opt. Lett. 32, 3002–3004. (2007)

[22] Y. Xu, L. V. Wang "Time reversal and its application to tomography with diffracting sources". Phys. Rev. Lett. 92, 033902. (2004)

[23] B. E. Treeby, E. Z. Zhang, B. T. Cox "Photoacoustic tomography in absorbing acoustic media using time reversal". Inverse Probl. 26, 115003. (2010)

[24] G. Paltauf, J. A. Viator, S. A. Prahl, S. L. Jacques "Iterative reconstruction algorithm for optoacoustic imaging". J. Acoust. Soc. Am. 112, 1536. (2002)

[25] M. H. Xu and L. H. V. Wang “Photoacoustic imaging in biomedicine”, Review of Scientific Instruments, Vol. 77, 22, (2006)

[26] M. Xu and L. V. Wang “Universal back-projection algorithm for photoacoustic computed tomography”, Physical Review E, Vol. 71, 016706, (2005)

[27] G. Paltauf, R. Nuster, and M. Burgholzer “Weight factor for limited angle photoacoustic tomography”, Phys. Med. Biol.. 54(11):3303-3314. (2009)

[28], W. L. Kiser, D. R. Reinecke, G. A. Kruger, K. D. Miller “Thermoacoustic Molecular Imaging of Small Animals. Molecular Imaging”. 2:113–123 (2003)

[29] R. A. Kruger, C. M. Kuzmiak, R. B. Lam, D. R. Reinecke, S. P. Del Rio, D. Steed “Dedicated 3D photoacoustic breast imaging”. Medical Physics.40. (2013)

[30] G. Paltauf., R. Nuster, M. Haltmeier and P. Burgholzer , “Photoacoustic tomography using a Mach-Zehnder interferometer as acoustic line detector”, Appl.Opt. 46, 3352-3358 (2007)

[31] P. C. Beard, F. Perennes, T. N. Mills “Transduction mechanisms of the Fabry-Perot polymer film sensing concept for wideband ultrasound detection”. IEEE Trans Ultrason Ferroelectr Freq Control. 46:1575–1582 (1999)

[32] E. Zhang, J. Laufer, P. Beard “Backward-mode multiwavelength photoacoustic scanner using a planar Fabry-Perot polymer film ultrasound sensor for high-resolution three-dimensional imaging of biological tissues”. Appl Opt47:561–577. (2008)

[33] Y. Wang, T. N. Erpelding, L. Jankovic, Z. Guo, J.-L. Robert, G. David, and L. V. Wang, “In vivo three-dimensional photoacoustic imaging based on a clinical matrix array ultrasound probe”, Journal of Biomedical Optics, Vol. 17, 061208-1 (2012)

[34] J. Gamelin “Curved array photoacoustic tomographic system for small animal imaging”. J Biomed Opt.13:024007 (2008)

[35] S. Gratt, G. Würzinger, R. Nuster and G. Paltauf”Free beam Fabry-Perot interferometer as detector for photoacoustic tomography”. European Conferences on Biomedical Optics. ed. International Society for Optics and Photonics, , (2013)

[36] C. H. Sherman and J. L. Butler, ‘Transducer and array for underwater sound’. Springer (2008)

[37] A. S. Fiorillo “A P(VDF-TrFE)-based integrated ultrasonic transducer”. In: Sensors and Actuators A: Physical 22.1, pp. 719-725 (1990)

[38] Q. Q. Zhang ”High frequency broadband PZT thick film ultrasonic transducers for medical imaging applications”. In: Ultrasonics 44, e711 - e715 (2006)

[39] Y. Xu, L. V. Wang, G. Ambartsoumian, P. Kuchment “Reconstructions in limited-view thermoacoustic tomography”. Medical Physics.31:724–733 (2004)

[40] M. Haltmeier, O. Scherzer, P. Burgholzer, and G. Paltauf “Thermoacoustic computed tomography with large planar receivers”. Inverse Problems. 20:1663-73 (2004)

[41] X. Lurton 2An Introduction to Underwater Acoustics2, XXXVI, 724 p. 32 illus. in color., Hardcover, ISBN: 978-3-540.78470-7 (2010)

[42] S. Gratt, R. Nuster, G. Wurzinger, M. Bugl, G. Paltauf “64-line-sensor array: fast imaging system for photoacoustic tomography”, SPIE Proceedings, Vol. 8943, **(**2014)

[43] B. Cox, P. Beard ”The frequency-dependent directivity of a planar Fabry-Perot polymer film ultrasonic sensor” IEEE Transitions on ultrasonics, ferroelectrics and frequency control, Vol. 54 (2007)

[44] M. Holotta, H. Grossauer, C. Kremser, P. Torbica, J. Völkl, G. Degenhart, R. Esterhammer, R. Nuster, G. Paltauf, and W. Jaschke “Photoacoustic tomography of ex vivo mouse hearts with myocardial infarction”. J. Biomed. Opt. 16, 036007 (2011)